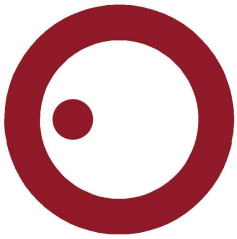

escola superior de tecnologia e gestão
instituto politécnico de leiria

Polytechnic of Leiria
School of Technology and Management
Department of Electrical and Electronics Engineering
Master in Electrical and Electronic Engineering – Electronics and Telecommunications

SWEPT-TIME DELAY CROSS-CORRELATION RADAR AT 24/28 GHZ

ANDRÉ FERREIRA SARDO

Leiria, April of 2020

This page is intentionally left blank.

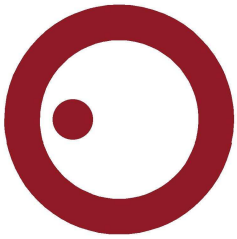

escola superior de tecnologia e gestão
instituto politécnico de leiria

Polytechnic of Leiria
School of Technology and Management
Department of Electrical and Electronics Engineering
Master in Electrical and Electronic Engineering – Electronics and Telecommunications

SWEPT-TIME DELAY CROSS-CORRELATION RADAR AT 24/28 GHZ

ANDRÉ FERREIRA SARDO
Number: 2172250

Dissertation supervised by Professor Rafael F. S. Caldeirinha (rafael.caldeirinha@ipleiria.pt).

Leiria, April of 2020

This page is intentionally left blank.

ACKNOWLEDGEMENTS

I would first like to express my gratitude towards my advisers, Professor Rafael Ferreira da Silva Caldeirinha, Professor Hugo Miguel Cravo Gomes and Nuno Ricardo Cordeiro Leonor for the continuous guidance and availability, allowing me to complete this dissertation.

I would also like to thank the School of Technology and Management of the Polytechnic of Leiria and the Instituto de Telecomunicações - Leiria (IT - Leiria) for providing me access to the laboratory facilities, including the necessary radio equipment to conduct the measurements for this work and the project RETIOT (POCI-01-0145-FEDER-016432) for funding the research performed during this work. Partial funding was also provided by Research and Technological Development Incentive Scheme CO-PROMOTION - Centro2020 - P2020 - European Regional Development Funds, under project RADAVANT - Radar for Detection and Avoidance in Unmanned Aerial Vehicles (PI nr. 033907).

I would like to thank the members of the Antenna and Propagation research group at IT - Leiria, especially Mário Vala and Wilson Conniott, for their constant availability to help and for providing a good working environment.

Finally, a special thank you for my parents and sister for always being there for me and supporting me.

This page is intentionally left blank.

ABSTRACT

Radar applications can be found today in many sectors of the industry and the number of implemented systems will keep increasing over time. Detecting and measuring the distance of an object with more accuracy and reliability becomes a complex task as possible interference sources are increasingly being deployed. Frequency-Modulated Continuous-Wave (FMCW) radars, simple and commonly used in the automotive industry, for example, suffer significantly from neighbouring FMCW radars, as they can corrupt each other's results and produce false positives or limit their ability to detect weaker reflections.

This project aims at the improvement of an existing radio channel sounder, as well as transitioning the system into a radar topology for target identification. The modular radar architecture allows the integration of different Radio Frequency (RF) stages present in the research group. The radar implements the Swept-Time Delay Cross-Correlation (STDCC) technique of Pseudo-Noise (PN) sequences, where amplitude and *Doppler* information can be extracted from multipath components, characterising the radio channel obstacles. The radar parameters can be easily adjusted on-the-fly to the environment being measured. A new RF front-end was developed at 28 GHz using X-MWblocks from X-Microwave, a modular designing and prototyping system for RF products. The baseband sequence generation has been implemented into an all-digital Field-Programmable Gate Array (FPGA) based system and tested in a controlled environment against a Commercial off-the-shelf (COTS) FMCW radar.

Keywords: Radar, Channel sounder, Sliding correlation, Pseudo-random sequences, RF front-end, Power Delay Profile, Multipath, Target identification.

This page is intentionally left blank.

TABLE OF CONTENTS

Acknowledgments i

Abstract iii

Table of Contents v

List of Figures vii

List of Tables xi

List of Acronyms xiii

1 INTRODUCTION 1

1.1 Background . . . 1

1.2 Aims and objectives . . . 1

1.3 Thesis Structure . . . 2

2 STATE OF THE ART 3

2.1 Radar principle . . . 3

2.2 Radio channel propagation . . . 3

2.2.1 Channel Functions . . . 4

2.2.2 Multipath . . . 4

2.3 Propagation channel fading . . . 6

2.3.1 Large scale fading . . . 6

2.3.2 Small scale fading . . . 6

2.3.3 Doppler shift . . . 7

2.3.4 Temporal scattering . . . 7

2.3.5 Transfer function . . . 8

2.4 Channel Sounding . . . 9

2.4.1 Direct periodic pulses . . . 9

2.4.2 Frequency domain . . . 10

2.4.3 Pulse compression . . . 11

2.5 Interim conclusions . . . 13

3 STDCC PRINCIPLE 15

3.1 Underlying principle . . . 15

3.1.1 Pseudo-noise sequence generation . . . 15

3.1.2 Autocorrelation of PN sequences . . . 16

3.1.3 Power Delay Profile and Multipath Phase Response . . . 17

3.1.4 Sounder parameters . . . 19

3.1.5 Co-existence with FMCW . . . 20
3.2 Interim conclusions . . . 23

4 IMPLEMENTATION OF A STDCC RADAR 25
4.1 Channel sounder . . . 25
4.1.1 Sequence generation . . . 25
4.1.2 RF stage . . . 27
4.1.3 6 GHz intermediate stage . . . 28
4.1.4 Sequence correlation . . . 29
4.2 Reconfiguration to radar . . . 30
4.3 Preliminary assessment of radar performance . . . 31
4.4 Calibration inside anechoic chamber . . . 32
4.5 Moving target . . . 34
4.5.1 Controlled environment . . . 34
4.5.2 Highly dense clutter environment . . . 35
4.6 Interim conclusions . . . 36

5 RADAR IMPROVEMENTS 37
5.1 A new RF frontend at 24/28 GHz . . . 37
5.1.1 X-Microwave Building Block System . . . 37
5.1.2 Calibration . . . 39
5.1.3 Measurement trials and results . . . 39
5.2 Baseband improvement based on FPGA and comparison with COTS solutions . . . 40
5.2.1 Radar Topology . . . 40
5.2.2 All-Digital Baseband . . . 42
5.2.3 Practical Implementation and Performance Analysis . . . 43
5.2.4 Comparison with commercial FMCW radar . . . 46
5.3 Interim conclusions . . . 49

6 CONCLUSION 51
6.1 Summary of results . . . 51
6.2 Published Works . . . 52
6.3 Future work . . . 52

BIBLIOGRAPHY 55

DECLARATION 59

LIST OF FIGURES

Figure 1 Example of a radar scenario. 3
Figure 2 Function relationships of randomly time-variant channels. . 4
Figure 3 Representation of direct and multipath signals. 5
Figure 4 Representation of a radio channel impulse response. 9
Figure 5 Block diagram of a periodic pulse system. 10
Figure 6 Block diagram of a frequency sweeping channel sounder. . . 10
Figure 7 Channel sounder using a VNA (image extracted from the work presented in [17]) 11
Figure 8 Pulse compression measurement system. 11
Figure 9 Channel sounder using the sliding correlation principle (image extracted from the work presented in [18]). 12
Figure 10 Channel sounder using the sliding correlation principle (image extracted from the work presented in [21]). 12
Figure 11 Example of a PN sequence generator. 15
Figure 12 Auto-correlation of a PN sequence. 16
Figure 13 Coherent IQ block diagram of a receiver. 17
Figure 14 Maximum unambiguous distance and trackable object speed vs. sequence length. 20
Figure 15 Cross-correlation simulation of identical sequences with 50 ns delay. 21
Figure 16 Cross-correlation simulation of sequences with 20, 50 and 80 ns delay with 3 dB, 6 dB and 10 dB attenuation, respectively. 21
Figure 17 Cross-correlation simulation of a PN sequence with a FMCW signal. 22
Figure 18 Cross-correlation simulation of a PN sequence with a FMCW signal and multiple PN sequences. 22
Figure 19 Channel sounder transmitter block diagram 25
Figure 20 Channel sounder receiver block diagram. 26
Figure 21 Spectrum of a 2 GHz signal generated by the RF2052. . . . 27
Figure 22 Spectrum of a 1 GHz PN sequence after after amplification and filtering. 27
Figure 23 TX (left) and RX (right) RF front-ends at 18.6 GHz. 28
Figure 24 Correlation result between identical sequences. 29
Figure 25 Radar block diagram. 30
Figure 26 Radar preliminary test of a single metallic pole. 31

Figure 27 Anechoic chamber calibration setup. 32
Figure 28 Radar calibration inside the anechoic chamber: (a) direct antennae coupling, (b) plus reflection from a single metallic pole, and (c) normalised reflection from the pole to the coupling component. 33
Figure 29 Moving target measurement setup. 34
Figure 30 Measurement results for the case of a forward and back moving person in the radio path between the sounder and a metallic pole, inside the anechoic chamber: (a) absolute time delay and distance; and (b) long-term averaged radial velocity evaluation 35
Figure 31 Absolute time delay and distance of measurement result for the case of a forward and back moving metallic plate in a cluttered environment: (a) full result; and (b) maximum values. 36
Figure 32 Long-term averaged radial velocity evaluation of measurement result for the case of a forward and back moving metallic plate in a cluttered environment 36
Figure 33 The complete 27 GHz RF Frontend using X-Microwave Innovative Modular Building Block System. 37
Figure 34 The complete 28 GHz channel sounder: (a) transmitter and (b) receiver block diagrams, respectively. 38
Figure 35 Relation between attenuation and correlation amplitude . . 39
Figure 36 5G use case - factory of the future (or Industry 5G). 40
Figure 37 Measured power delay profile for all azimuth angles as a function of: (a) azimuth angle over absolute delay; and (b) absolute delay. 40
Figure 38 Block diagram of the STDCC radar architecture. 41
Figure 39 STDCC radar baseband. 43
Figure 40 Photography of the STDCC radar prototype. 44
Figure 41 (a) Radar 360° setup with 7 poles, (b) Radar 360° setup with 8 poles 45
Figure 42 Experimental results for multiple poles scenario: (a, c) waterfall PPI plots and (b, d) polar PPI plots for the 7 poles setup and 8 poles setup, respectively. 45
Figure 43 (a) Radar benchmark setup, (b) Two-pole experimental setup assembled inside the anechoic chamber. 46
Figure 44 Experimental results for one-pole scenario: (a, c) waterfall PPI plots and (b, d) polar PPI plots for, the STDCC and FMCW radars, respectively. 47

Figure 45 Experimental results for two-pole scenario: (a, c) waterfall PPI plots and (b, d) polar PPI plots, for the STDCC and FMCW radars, respectively. 48

This page is intentionally left blank.

LIST OF TABLES

Table 1 STDCC channel sounder parameters. 19
Table 2 Radio system parameters. 34

This page is intentionally left blank.

LIST OF ACRONYMS

5G NR	5G New Radio.
ADC	Analog-to-Digital Conveter.
AWGN	Additive White Gaussian Noise.
CNC	Computer Numerical Control.
COTS	Commercial off-the-shelf.
DAC	Digital-to-Analog Conveter.
DAQ	Data aquisition.
DPG2	Data Pattern Generator 2.
FFT	Fast Fourrier Transform.
FM	Frequency Modulation.
FMCW	Frequency-Modulated Continuous-Wave.
FoF	Factories of the Future.
FPGA	Field-Programmable Gate Array.
I	In-Phase.
IF	Intermediate Frequency.
LNA	Low Noise Amplifier.
LO	Local Oscillator.
LOS	Line Of Sight.
LVDS	Low-Voltage Differential Signaling.
MLSR	Maximal Length Shift Register.
MMCM	Mixed-Mode Clock Manager.
MPC	Multipath Component.
MPR	Multipath Phase Response.
NLOS	Non Line Of Sight.
OFDM	Orthogonal Frequency Division Multiplexing.
PDP	Power Delay Profile.
PLL	Phase Locked Loop.
PN	Pseudo-Noise.

PPI	Plan Position Indicator.
Q	Quadrature.
RF	Radio Frequency.
ROM	Read-Only Memory.
SNR	Signal-to-Noise Ratio.
SSB	Single Side Band.
STDCC	Swept-Time Delay Cross-Correlation.
US	Uncorrelated Scattering.
VCO	Voltage-controlled oscillator.
VNA	Vector Network Analyzer.
WSS	Wide Sense Stationary.
WSSUS	Wide Sense Stationary and Uncorrelated Scattering.
X-MWblocks	X-Microwave Innovative Modular Building Block System.
XOR	Exclusive Or.

1 INTRODUCTION

1.1 BACKGROUND

Radar applications can be found in many sectors of the industry, from ground and marine traffic control to space exploration, from recreational to medical, from military to automotive. The simple act of detecting and measuring the distance of an object, which may or may not be in line of sight, with increasingly more accuracy and speed requires complex and powerful systems, pushing existing technology to the limits. Depending on the application, many specifications must be defined, such as: maximum detectable distance for long range target identification; minimum spacial resolution for objects in close proximity; maximum *Doppler* and speed detection for dynamic and moving targets; interference immunity due to the increased number of simultaneous radar applications; maximum angular range detection for a wider field of view; among others. These specifications are important to consider when designing and implementing a radar system.

The increased use of Frequency-Modulated Continuous-Wave (FMCW) based radars and sensors, such as in the large scale deployment in the automotive industry, poses a significant problem in regards to interference between systems. A radar transmitting a continuous signal can corrupt a neighbouring radar received signal, increasing the risk of occurrence of false positives and reducing the sensitivity towards weaker reflections [1, 2]. As such, Swept-Time Delay Cross-Correlation (STDCC) based radars gain an advantage over FMCW radars due to the auto-correlation properties of the transmitted signals. A maximum peak value is only obtained when the received signal is identical to the transmitted signal and minimum value in other cases.

1.2 AIMS AND OBJECTIVES

Considering that a channel sounder has already been developed and implemented at IPLeiria [3–7], this work aims at improving and migrating the system into a radar topology, capable of both target detection and identification. The existing modular channel sounder utilises the STDCC technique of Pseudo-Noise (PN) sequences for channel measurement and characterisation, providing a plethora of information in

regards to the channel behaviour and its obstacles, while also being resilient towards commonly used FMCW signals.

The objectives defined for this work comprise of: understanding the existing channel sounder and the underlying principle of the STDCC technique; reconfiguring the system into a monostatic radar topology; integration of 24-28 GHz Radio Frequency (RF) frontends for 5G New Radio (5G NR) utilisation; miniaturisation of the baseband sequence generation by means of employing an Field-Programmable Gate Array (FPGA); comparing the performance with existing Commercial off-the-shelf (COTS) solutions; and disseminate the work being performed in conferences through scientific publications.

1.3 THESIS STRUCTURE

This document is divided into 6 chapters with the following organisation:

Chapter 1 aims to situate this dissertation, briefly explaining its purpose and structure.

Chapter 2 presents the current state of the art of channel sounding and radar technology, the different technologies and strategies used, including some implemented systems in the literature.

Chapter 3 aims to explain the STDCC technique, how a PN sequence is generated and its properties, as well as its immunity against interference from currently widely used FMCW based radar.

Chapter 4 explains the inner workings of the STDCC channel sounder that was previously implemented and its transition into a mono-static radar topology. Preliminary measurements of a simple scenario is presented, as well as a system calibration.

Chapter 5 consists in presenting a new RF front-end ranging from 24 to 28 GHz that was developed and measurement trials carried out in a harsh factory-like environment.

Chapter 6 presents the transition of the baseband PN sequence generation into an FPGA based system, including measurements and comparison with a COTS solution.

Chapter 7 will present a brief analysis of the work that was developed and conclusions based on the obtained results will be discussed. Finally, suggestions for future work will be mentioned.

2

STATE OF THE ART

This chapter will address the characteristics of a radio channel, the principle behind channel sounding and its importance in radar technology. This includes various system topologies that have been implemented in the literature to obtain the impulse response of a wireless channel.

2.1 RADAR PRINCIPLE

A radar consists of the transmission and reception of a radio signal into a radio channel, with the purpose of detection and ranging of obstacles within. The transmitted signal travels inside the radio channel and is reflected by a target, which then returns to the radar, as shown in Fig. 1. The received signal contains important information regarding the target, such as the delay, in relation to the transmitted signal, and frequency shift. The delay corresponds to the travel time the radio wave takes to reach the target and travel back, corresponding to the distance at which the target is located from the transmitter. The frequency shift is caused by the *Doppler* effect and it is related to the velocity of the target [8].

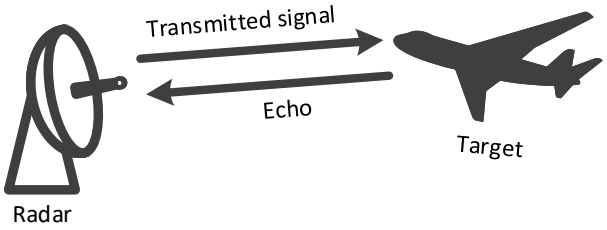

Figure 1: Example of a radar scenario.

2.2 RADIO CHANNEL PROPAGATION

Wireless channels are very unpredictable and difficult to characterise. They are randomly variant in time, unlike wired connections, due to interferences, noise and multipath components.

2.2.1 *Channel Functions*

Mathematical functions have already been established in the literature to describe the relationship between the input and output signals of a radio channel. Bello [9] has defined four main functions:

- Time-variant impulse response function: $h(t,\tau)$;
- Time-variant transfer function: $H(t,f)$;
- Scattering function: $S(v,\tau)$;
- Frequency shift transfer function: $H(v,f)$.

Where t represents time, τ represents propagation delay, f is the frequency of the transmitted signal and v is the *Doppler* frequency.

Physical radio propagation channels are assumed to be approximately stationary for sufficiently long time intervals (t), characterising them as Wide Sense Stationary (WSS), where the autocorrelation functions of the channel at instants t_1 and t_2 only depend on the time variation $t = t_2 - t_1$.

Radio propagation channels are also assumed to be randomly scattering, or Uncorrelated Scattering (US), where each multipath component and respective delays are uncorrelated between each other.

By assuming the propagation channel as WSS and US, or Wide Sense Stationary and Uncorrelated Scattering (WSSUS), the Fourier Transform and its inverse can be applied to obtain the desired function, as shown in Fig. 2 [3, 9, 10].

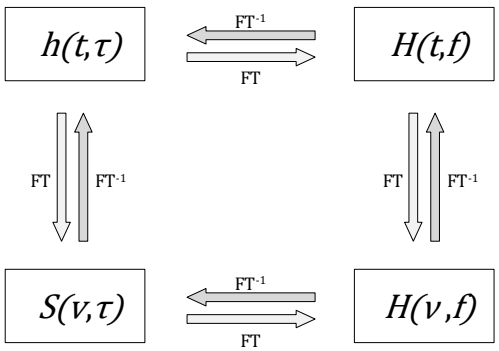

Figure 2: Function relationships of randomly time-variant channels.

2.2.2 *Multipath*

Multipath is an important characteristic in wireless channels, where an antenna receives two or more signals coming from different paths. This phenomenon can

be caused by reflection and refraction from a multitude of obstacles, such as the ionosphere, mountains, buildings, vegetation, vehicles, and more [11]. The effects of multipath components include constructive and destructive interference on the signal, as well as phase shifting.

A visible effect of multipath components can be seen on analog television transmission systems, where a "ghosting" effect appears. Frequency Modulation (FM) Radio transmission also suffer from multipath by causing apparent echoing of the original signal. On digital systems, the multipath effect can cause substantial loss on maximum available throughput. A simplified illustration is depicted in Fig. 3.

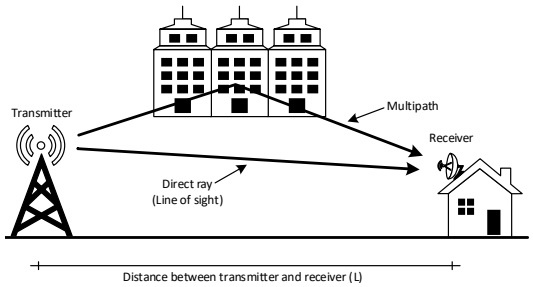

Figure 3: Representation of direct and multipath signals.

If a continuous signal is transmitted in this scenario while assuming that the propagation channel is static, thus presenting no variation over time, the equations 1 and 2 can be obtained. A single Line Of Sight (LOS) signal and a single multipath, or Non Line Of Sight (NLOS), signal are assumed for these equations [12].

$$S_{LOS}(t) = A_{LOS}\cos\left(2\pi f_c t + \varphi_{LOS}\right) \tag{1}$$

$$S_{MP}(t) = A_{MP}\cos\left(2\pi f_c t + \varphi_{MP}\right) \tag{2}$$

Where:

S_{LOS} is the line of sight signal;

S_{MP} is the multipath signal;

A_{LOS} is the received amplitude of the line of sight signal;

A_{MP} is the received amplitude of multipath signal;

f_c is the carrier frequency of the signal;

φ_{MP} is the received phase of the line of sight signal;

φ_{MP} is the received phase of multipath signal.

In this case, the multipath signal may differ from the LOS signal in regards to received amplitude, which can be influenced by different attenuations from the propagation medium. The signal may also differ in regards to received phase due to the difference in travel distance and reflections from obstacles.

2.3 PROPAGATION CHANNEL FADING

The fading of a propagation channel directly affects the quality of the reception in a given system. The fading effects can be classified in two scales: large scale fading and small scale fading.

2.3.1 *Large scale fading*

The concept of large scale fading essentially represents the average attenuation of the signal while travelling a long distance radio channel, such as distances corresponding to hundreds of wavelengths (λ). The degradation of the signal caused by the presence of objects of large proportions is called shadowing, where the size of the obstacle intercepts a large area, creating a "shadow" over the receiving antenna.

An ideal signal propagating through vacuum, or free space, would suffer an attenuation proportional to the square of the distance travelled. However, in physical channels, the energy of these signals are absorbed and reflected by the atmosphere and obstacles, man-made or natural. This effect limits the overall performance of a system similar to the one described previously. The fluctuations of this value occur due to the shadowing effect, tied to the physical phenomenon of diffraction. This phenomenon occurs when radio signals travel around corners and edges of buildings.

2.3.2 *Small scale fading*

In addition to the losses associated to long travelled distances, fluctuations also occur in proximity of the receiver, corresponding to units of wavelengths. Small scale fading includes the variation in received power, temporal spreading and spectral spreading due to the *Doppler* effect.

The fact that a signal can possess multiple travel paths to reach the receiver, where each path can suffer a plethora of physical phenomenons (reflection, diffraction, scattering), originates multiple copies of the signal on the receiver, each with different delays, amplitudes or even phase shifts [13]. All of these signals will converge on the receiver, originating constructive or destructive interference.

2.3.3 *Doppler shift*

Doppler shift is characterised by the *Doppler* scattering of dynamic or time-variant channels. The movement of objects, or even transmitter/receiver movement, are the principal cause of *Doppler* spreading [13].

Doppler shift occurs when the receiver is in movement in relation to a static transmitter. In this situation, the received signal is modulated in frequency according to the direction of the movement. Signal echoes that arrive from paths opposing the direction of the receiver's movement will appear to have a higher frequency, whilst signal echoes arriving from paths with the same direction will appear to have lower frequencies.

Similarly, any mobile passive scattering object in the channel path, capable of retransmitting an incident signal by reflection, refraction or other physical phenomenon, will cause the same frequency modulation over on said signal. As multiple signals arrive at the receiver, each with their own *Doppler* effects, the resulting sum of these signals will provoke a varying amplitude over time.

2.3.4 *Temporal scattering*

Another effect that is manifested on the receiver is temporal scattering, which is caused by different multipath signals arriving at different instants of time in relation to the direct (LOS) component. The delay between the first and the last components, corresponding to the shortest and longest paths, is denoted as maximum excess delay (T_M).

Considering a system that is operating on a given propagation channel, where the necessary time to transmit a symbol (T_S) is greater than the maximum excess delay ($T_S > T_M$), then the propagation channel presents an approximately constant attenuation since every multipath component will arrive during the time window of said symbol. In the frequency domain, the previous statement is equivalent to stating that the signal's bandwidth (B_S) is smaller than the coherence bandwidth (B_C), that is, $B_S < B_C$.

The coherence bandwidth of a radio channel is a statistical quantity that measures the frequency ranges which, when transmitted, suffer amplitude losses approximately constant. By contrast, if $T_S < T_M$ or $B_S < B_C$ is verified, then it is considered that the channel originates attenuations on the transmitted signal that are selective in frequency [13].

2.3.5 *Transfer function*

As a radio channel is a dynamic environment, where various objects capable of reflection and diffraction are present, it is considered to be non-stationary. However, it is possible to create mathematical functions, capable of representing these random alterations of the radio channel, by representing them as randomly time-variant linear filters [9].

By assuming that the radio channel variations are much slower compared to the data acquisition system and is a WSSUS channel, the impulse response of the channel can be defined by the equation 3:

$$h(t,\tau) = \sum_{i=1}^{N} a_i(t) e^{-j\theta_i(t)} \delta(\tau - \tau_i(t)) \tag{3}$$

Where:

- $h(t,\tau)$ is the time-variant impulse response of the radio channel;
- $a_i(t)$ is the time-variant magnitude of each multipath component, representing free space loss and other losses of the channel;
- $\theta_i(t)$ is the time-variant phase of each multipath component, representing free space phase shift and other phase shifts of the channel;
- $\tau_i(t)$ is the time-variant exceeding delay of the multipath components of the radio signal.

This equation approximately represents the arrival of LOS signal, followed by possible multipath signals with delay τ_i, where each signal have its respective attenuation, delay and phase shift. In other words, it represents the response of a pulse with an unitary time t, assessed at the delay τ after the pulse was originated [14]. Since channels are naturally dynamic, an impulse response is only valid for the instant in time it was acquired. As such, the impulse response can be generically represented by Fig. 4.

Obtaining the impulse response of a channel is directly related with the concept of transfer functions, where an output signal ($y(t)$) can be obtained by convolving the input signal ($x(t)$) with the impulse response ($h(t,\tau)$). By obtaining the output signal, if the input signal is known, the impulse response can be extrapolated.

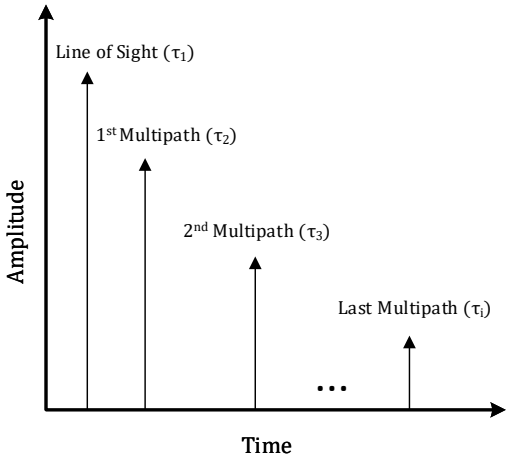

Figure 4: Representation of a radio channel impulse response.

2.4 CHANNEL SOUNDING

Channel sounding consists in understanding the behaviour of a wireless channel, with the help of measurement equipment, specifically developed for channel characterisation. These systems aim to measure the transfer function of a given wireless channel. Knowing the transfer function of a channel allows us to understand the effects of said channel, such as delay, attenuation, multipath echoes and phase shift on a transmitted signal. With this information, system designers can decide on the best radio architecture and modulation to apply in their designs, maximising throughput and reliability.

Various channel sounding techniques exist in the literature, namely i) direct periodic pulses; ii) frequency domain or Vector Network Analyzer (VNA); iii) Pulse compression; and iv) STDCC based systems [12]. Each technique have advantages and disadvantages. However, the focus of this dissertation is to improve upon the existing spread spectrum sliding correlator channel sounder, due to the properties of spread spectrum transmissions.

2.4.1 *Direct periodic pulses*

The simplest channel sounding technique is the direct RF pulse system, where a pulse generator is fed into an RF switch, allowing a signal generator to pass through an amplifier to then be transmitted. At the receiver, the signal is filtered and amplified before being detected by an envelope detector and displayed on an oscilloscope. A typical system diagram is shown in Fig. 5 [13, 15].

Such systems are simple to implement with few components, but to obtain high resolution multipath information, very high speed and expensive components must

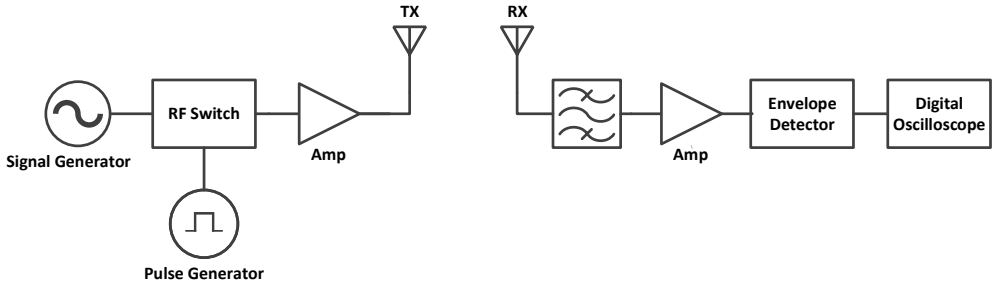

Figure 5: Block diagram of a periodic pulse system.

be used. These transmitters require a high peak-to-average-power ratio and the dynamic range is reduced due to their high sensitivity to interference and noise, limiting the ability to detect weaker multipath signals [16].

2.4.2 *Frequency domain*

A channel sounder that utilizes frequency sweeping to obtain channel information commonly resorts to employing a VNA. A frequency sweep in discrete intervals is made to obtain the complex frequency response of the channel over the desired frequency interval. The inverse Fourier Transform is applied to then obtain the desired impulse response, or Power Delay Profile (PDP), of the channel. This is also a simple system to implement, as shown in Fig. 6, limited by the frequency range of the VNA and oscillators. A high multipath resolution is achievable, depending only on the frequency step size. However, the step size and number of points used for the frequency sweep also dictate the time taken for a single sweep, as the inverse Fourier Transform is only applied at the end of each sweep. As such, this technique is only viable for channels that appear to be time-invariant for the duration of the sweep. *Doppler* spectra cannot be obtained by this method due to the discrete frequency sweeping nature of the VNA.

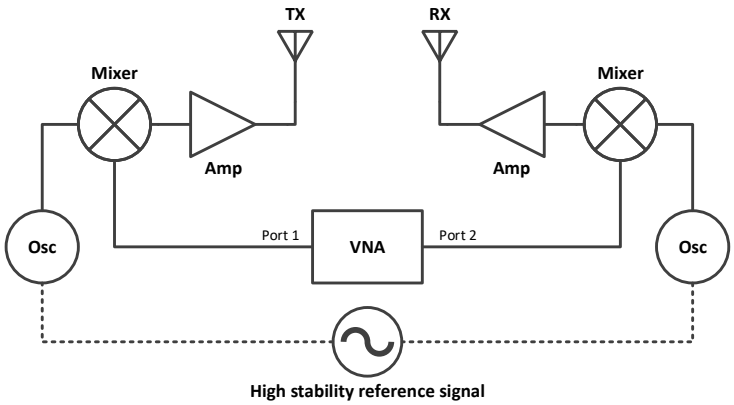

Figure 6: Block diagram of a frequency sweeping channel sounder.

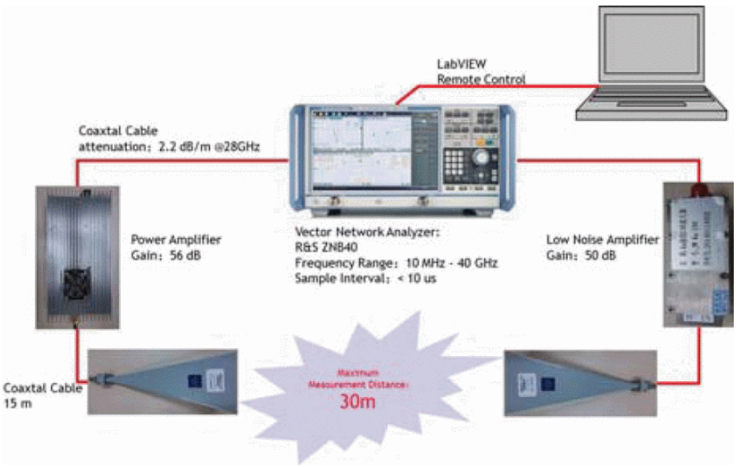

Figure 7: Channel sounder using a VNA (image extracted from the work presented in [17])

In [17], the authors present a VNA based channel sounder where no oscillators are used, as shown in Fig. 7. This was achieved by setting the centre frequency of the VNA directly to the measuring frequency of 28 GHz so an up-conversion is not necessary. A 1 GHz span of 200 sample points was used to obtain a 5 MHz bandwidth, corresponding to a maximum excess delay of 200 ns which then limits the maximum travel distance to 60 m.

2.4.3 *Pulse compression*

A pulse compression system takes advantage of the auto-correlation properties of White noise signals. Such signal, $n(t)$, can be used to excite a wireless channel and the result is cross-correlated with an identical, but time delayed, version of the transmitted signal, $n(t-\tau)$. The result of the correlation, $y(t)$, is proportional to the channel impulse response, $h(t,\tau)$, evaluated at a time τ, as shown in Fig. 8 [12].

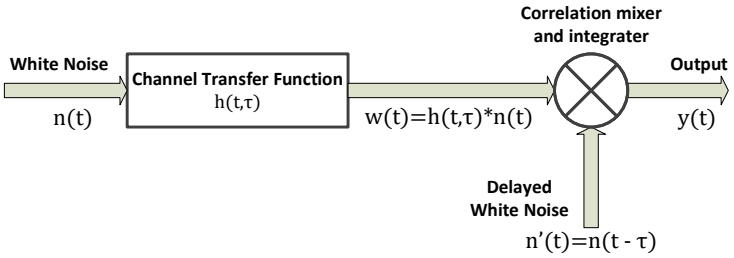

Figure 8: Pulse compression measurement system.

However, this system requires the knowledge a priori of the transmitted signal, which is not the case for white noise as it is, by definition, a random signal. In addition, the output of the system is a function dependent of τ, where τ is needed to be adjusted to measure all values of the transfer function $h(t,\tau)$. This would imply a significant required computing time, which would compromise real-time measurement of dynamic channels.

The limitations above can be eliminated by employing PN signals, which are deterministic sequences (can be known a priori) and have very similar auto-correlation properties to white noise signals. These properties will be explained in Chapter 3, where the sliding correlation technique will be presented.

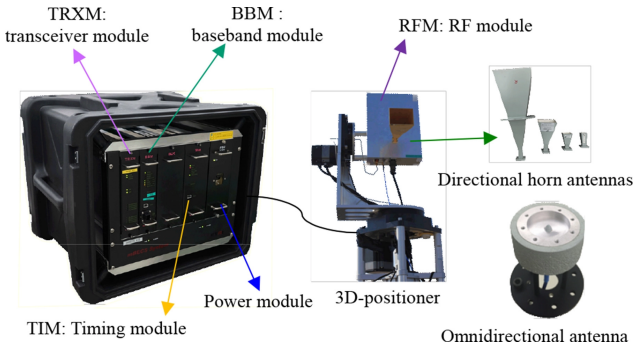

Figure 9: Channel sounder using the sliding correlation principle (image extracted from the work presented in [18]).

Numerous channel sounders using the sliding correlation principle have been presented in the literature. In [18], a wideband channel sounder operating at 28 GHz and 38 GHz is presented. Fig. 9 depicts the following modules of the sounder: a base band module, a transceiver module, a timing module, a 28/38 GHz RF module, and antennas. A 500 MHz bandwidth provides a multipath delay resolution of 2 ns. The sliding factor of the system is 12500 and a sequence with 4095 chips is used, providing a dynamic range of 72 dB.

In [19] and [20], a binary sequence with length of 2^{13} - 1 chips is transmitted at 60 GHz with 500 MHz bandwidth. This allows a multipath delay resolution of 2 ns and maximum non-ambiguous delay of 16.4 us. The results are sampled at a rate of 10 GS/s over periods of 50 us and stored for offline analysis.

The authors of [21] and [22] implemented a channel sounder at 2.6 GHz, transmitting a sequence with a length of 1023 bits. A bandwidth of 62.5 MHz is achieved

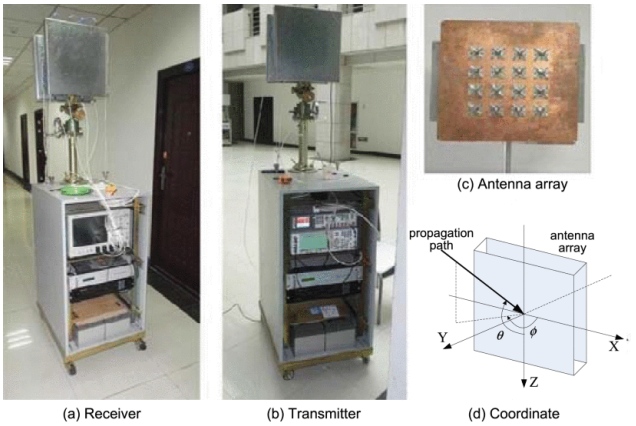

Figure 10: Channel sounder using the sliding correlation principle (image extracted from the work presented in [21]).

and the maximum detectable delay of 16.368 us. The sequence is transmitted by a 4x4 array of cross patches, as shown in Fig. 10, to capture the spatial signature of channels with different polarizations.

In [16], a PN sequence of 2047 chips in length is generated at a rate of 500 Mcps by an FPGA for a 2 ns time resolution. The channel sounder transmits the signal at 73 GHz and obtains both In-Phase (I) and Quadrature (Q) baseband components at the receiver by employing an IQ demodulation mixer at the down-conversion. The frequency offset of the sequence generated at the receiver is of 62.5 kHz, providing a sliding factor of 8000 and a 39 dB processing gain. The result on both branches are sampled at 1.5 GS/s independently.

2.5 INTERIM CONCLUSIONS

The characterisation of a radio channel has thoroughly been studied in the literature by exploring its components such as fading, multipath, scattering and *Doppler* Shift. Channel sounders are especially designed, by employing various types of equipments and topologies, to extract these characteristics. In the same fashion, radars also acquire channel information to consequently detect or track a defined target. Having a background on channel sounding techniques allows a better understanding of the behaviour of a radio channel for radar applications.

This page is intentionally left blank.

3

STDCC PRINCIPLE

3.1 UNDERLYING PRINCIPLE

Channel sounding based on the sliding correlation technique takes advantage of the auto-correlation properties of PN sequences. This chapter will explain the sequence generation process, its auto-correlation properties and resilience in regards to commonly used FMCW radar interference.

3.1.1 *Pseudo-noise sequence generation*

A PN sequence is a periodic binary sequence that is statistically similar to a purely random sequence of bits. Many types of PN sequences exist, however, the sequences which will be focused in this project are of the type Maximal Length Shift Register (MLSR) [3, 12, 14, 23–25].

Such sequences can be generated using the underlying principle shown in Fig. 11, by means of logic gates such as Exclusive Or (XOR), 1-bit shift registers and feedback taps, as in the generation of a *Fibonacci* sequence. These sequences have a periodic length of N chips, where $N = 2^n - 1$ and n being the number of shift registers.

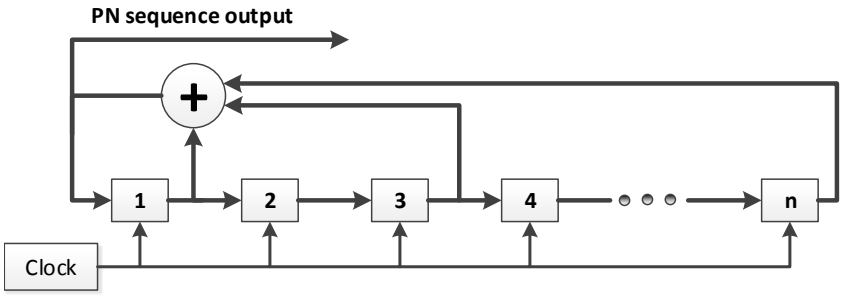

Figure 11: Example of a PN sequence generator.

The statistical distribution of ones and zeros is identical to a purely random sequence, with the exception where the number of ones is greater than the number of zeros by 1 unit, regardless of the sequence size.

3.1.2 *Autocorrelation of PN sequences*

PN sequences have specific properties which are of great interest in the present application. The auto-correlation of such a sequence is given by (4).

$$R_{xx}(\tau) = -\frac{1}{N}\sum_{l=-\infty}^{l=\infty}\left(1+\frac{1}{N}\right)\Delta\left(\frac{\tau - lNT_c}{T_c}\right) \tag{4}$$

$$\text{Where: } \Delta\left(\tfrac{\tau-lNT_c}{T_c}\right) = \begin{cases} 1-\frac{|\tau-lNT_c|}{T_c}, & |\tau - lNT_c| \leq T_c \\ 0, & |\tau - lNT_c| > T_c \end{cases}$$

T_c is the clock period, N is the PN sequence length, τ is the time delay and l defines the summation limits.

In order to have two sequences to "slide" against each other, the receiver PN sequence clock needs to be adjusted to a sightly slower rate than that of the PN sequence clock at the transmitter. The difference in frequency of these sequences described as the Slip rate, is denoted by,

$$f_{slip} = f_T - f_R \tag{5}$$

Where f_T is the transmitter PN chip frequency and f_R is the receiver PN chip frequency.

A maximum correlation amplitude will be obtained when both sequences are aligned in time, and a minima for all other cases due to the orthogonality properties of these sequences [25]. Hence, distinct multipath components obtained from the radio channel, will maximally correlate at different instants in time. Fig. 12 depicts the auto-correlation of a PN sequence.

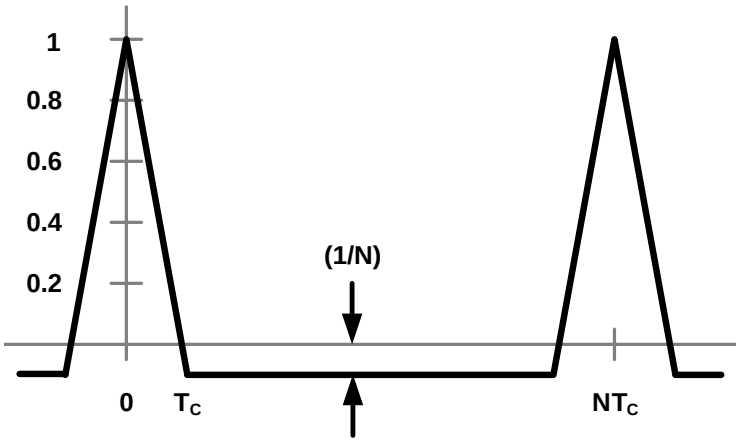

Figure 12: Auto-correlation of a PN sequence.

Despite the signal dispersion in time due to multipath, in the order of several nanoseconds, the use of STDCC effectively spreads out in time those components at the output of the correlator. The amount by which the correlation peaks are time dilated is described as sliding factor, denoted by (6).

$$k = \frac{f_T}{f_T - f_R} \tag{6}$$

Consequently, when considering a transmitter PN sequence clocked at 100 MHz and a receiver PN sequence clocked at 99.999 MHz, which yields a sliding factor of 100000, a 20 ns correlation pulse ($2T_c$) will be acquired as a 2 ms pulse, representing the effective time dilation. The baseband bandwidth of the channel sounder is equal to the slip rate.

3.1.3 *Power Delay Profile and Multipath Phase Response*

To be able to construct a PDP and Multipath Phase Response (MPR) from the radar, the acquisition of both magnitude and phase information of the channel impulse response is necessary. This can be achieved in a channel sounder by implementing a coherent receiver similar to the one shown in Fig. 13 [24].

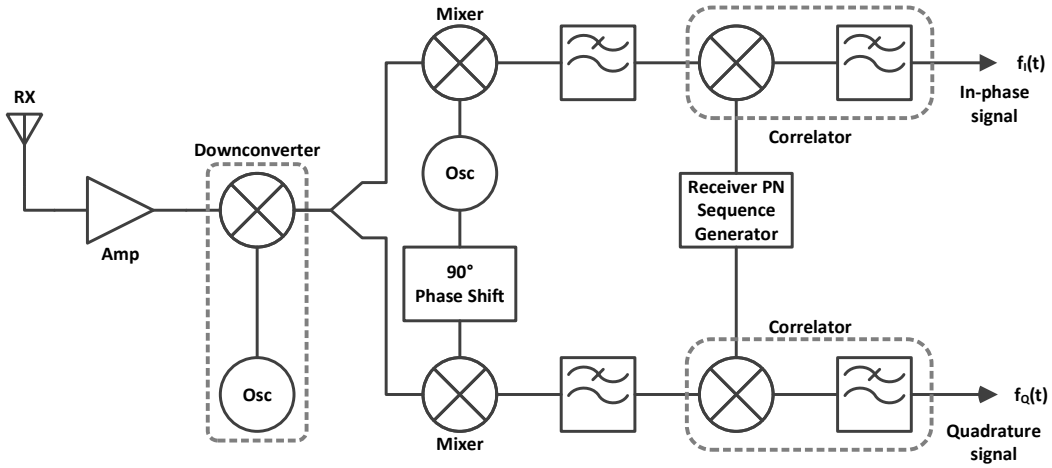

Figure 13: Coherent IQ block diagram of a receiver.

A sliding correlation channel sounder employing this architecture, with a perfect oscillator syncretisation between transmitter and receiver, can output a received signal mathematically represented by the equations 7 and 8 [24]:

$$V_T(t) = s(t)\cos(2\pi f_c t) \tag{7}$$

$$V_R(t) = \sum_i a_i(t)s(t - \tau_i(t))\cos(2\pi f_c t - 2\pi f_c \tau_i(t)) \tag{8}$$

Where:

$V_T(t)$ is the transmitted signal;

$s(t)$ is the PN sequence;

$V_R(t)$ is the receiver signal, representing the sum of the direct component and multipath components;

$a_i(t)$ is the amplitude variation over time of the multipath components;

$\tau_i(t)$ is the delay variation over time of the multipath components;

$s(t-\tau_i(t))$ is the PN sequence received by the multipath components and in this case, $\tau_i(t)$ represents a shift in position of the received sequence in relation to the transmitted sequence;

$2\pi f_c \tau_i(t)$ is the phase received by the multipath components, representing a phase shift of the received sequence in relation to the transmitted sequence;

At the output of the coherent receiver, both in-phase and quadrature signals can be obtained, represented by the equations 9 and 10 respectively [24].

$$f_I(t) = \sum_i a_i(t) R_s\left(\frac{t}{k} - \tau_i(t)\right) \cos\left(2\pi f_c \tau_i(t)\right) \tag{9}$$

$$f_Q(t) = \sum_i a_i(t) R_s\left(\frac{t}{k} - \tau_i(t)\right) \sin\left(2\pi f_c \tau_i(t)\right) \tag{10}$$

Where:

$f_I(t)$ is the correlated in-phase signal;

$f_Q(t)$ is the correlated quadrature signal;

$R_s\left(\frac{t}{k} - \tau_i(t)\right)$ is the auto-correlation of the PN sequence, dilated in time by the sliding factor k and analysed at the delay corresponding to each multipath component.

Finally, by combining these signals we can obtain the PDP of the channel and the MPR of the channel with the equations 11 and 12, respectively:

$$E(t) = |h(t,\tau)|^2 = f_I^2(t) + f_Q^2(t) \text{ scaled by k} \tag{11}$$

$$\theta(t) = \angle h(t,\tau) = \tan^{-1}\left(\frac{f_Q(t)}{f_I(t)}\right) \text{ scaled by k} \tag{12}$$

Where:

$E(t)$ is the PDP of the channel, which is equivalent to the square of the magnitude of the channel impulse response;

$\theta(t)$ is the time-variant phase response of the channel, which is equivalent to the phase of the channel impulse response;

The resulting PDP consists in a graph, scaled in time by the sliding factor k, presenting the received power and delay of each multipath components of the channel. The *Doppler* spectrum of the channel provides the spectrum broadening of the received signal caused by time-variant multipath components.

3.1.4 *Sounder parameters*

The parameters of a channel sounder implementing the STDCC technique have been defined by various authors [3, 12, 25–27] and is presented in Table 1.

Parameter	Expression
Chip period	$T_c = \frac{1}{f_c}$ seconds
PN sequence length	$N_{PN} = 2^n$ - 1 chips
PN sequence period	$T_{PN} = N_{PN}T_c$ seconds
RF bandwidth	$B_{RF} = 2f_c$ Hz
Baseband bandwidth	$B_{bb} = 2(f_T - f_R)$ Hz
Sliding factor	$k = \frac{f_T}{f_T - f_R}$
Dynamic Range	$D_R = 20\log_{10}(N_{PN})$ dB
Multipath temporal resolution	$\Delta\tau = 2T_c$ seconds
Multipath spatial resolution	$\Delta s = c\Delta\tau$ metres
Maximum delay	$\tau_{max} = N_{PN}T_c$ seconds
Maximum range	$s_{max} = c\tau_{max}$ metres
Maximum *Doppler* shift	$f_{Dmax} = \frac{f_c}{2kN_{PN}}$ Hz
Maximum target speed	$v_{max} = \frac{\lambda carrier}{2kN_{PN}T_c}$ m/s

Table 1: STDCC channel sounder parameters.

As shown in the table, the importance of the chip period and the sequence length is evident, as most parameters are dependent on them. The sliding factor defines

the scale at which the post-correlation spreading occurs and, as a consequence, the equipment needed for signal acquisition.

With these formulas, a relationship between the sequence length, slip rate, maximum radar distance and maximum trackable object speed can be observed. Fig. 14 represents these relationships for a sequence clocked at 1 GHz.

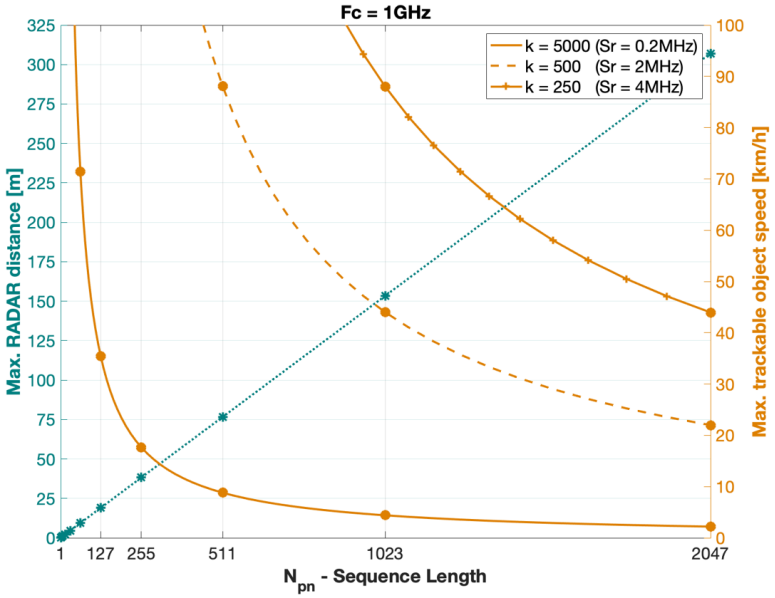

Figure 14: Maximum unambiguous distance and trackable object speed vs. sequence length.

As the sequence length increases, the maximum radar distance increases while the maximum trackable object speed decreases. This parameter also increases when the slip rate is greater. As such, the radar parameters should be set according to the scenario to be studied.

3.1.5 *Co-existence with FMCW*

As mentioned previously, the auto-correlation properties of PN sequences allows a channel sounder to be resilient against commonly used FMCW radar signals. If the received signal is not a copy of the transmitted signal, then the cross-correlation of these signals will result in a minimum value.

Simulations were performed to assess this statement by implementing the correlation of a sequence sliding across another. Two identical 7-bit PN sequences were generated with a clock rate of 100 MHz and one was delayed 50 ns from the other. The correlation result presents a maximum correlation peak corresponding to the instant in time at which the sequences are aligned, and a minimum value on other cases, as shown in Fig. 15.

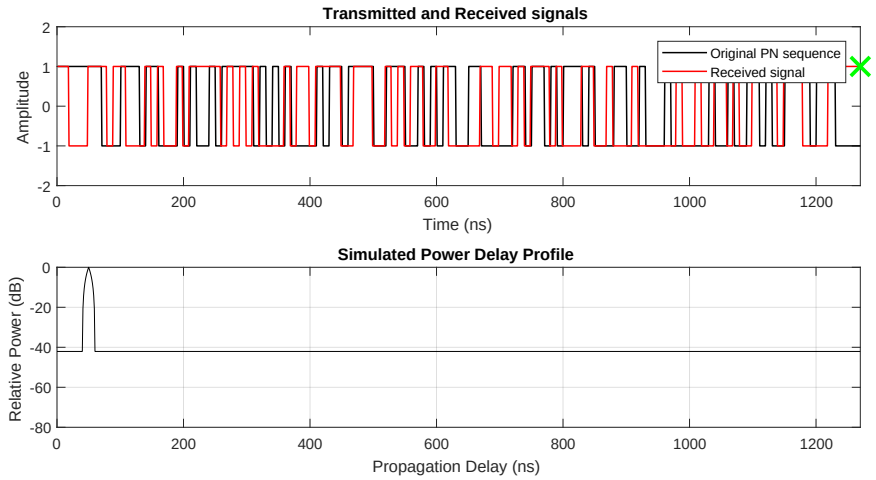

Figure 15: Cross-correlation simulation of identical sequences with 50 ns delay.

A normalised correlation peak can be observed at 50 ns, as expected, while the remaining values are -42 dB below. This is due to the dynamic range achieved by using 7-bit sequences, as $D_R = 20\log_{10}(2^7) \approx 42$ dB.

To verify the effect of multipath components, the same sequence was delayed again (100 ns and 200 ns) and summed to the previously generated sequence with 50 ns delay. To simulate the attenuation effect of signal propagation, attenuations of 3 dB, 6 dB and 10 dB were applied to the sequences. The results of Fig. 16 presents similarities with the previously simulation, where each correlation peak is located at the corresponding delay of each sequence (50 ns, 100 ns and 200 ns). In addition, each correlation peak also display the correct attenuation, while the resulting values are still at -42 dB.

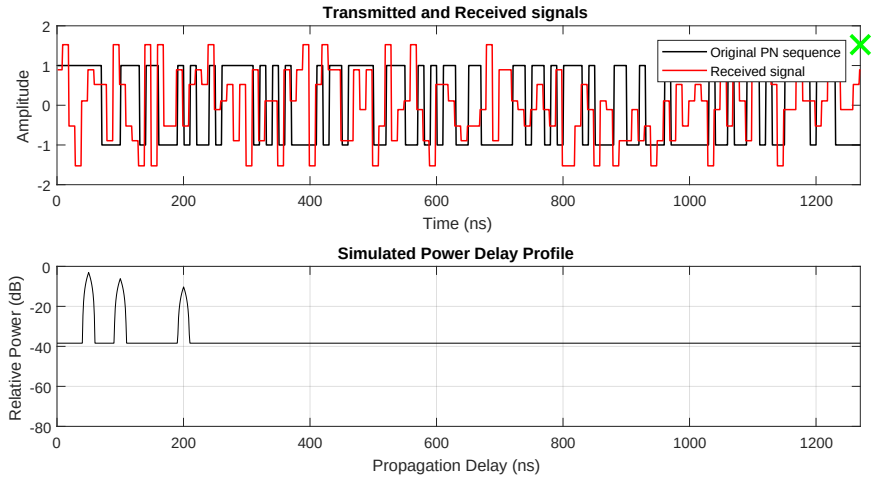

Figure 16: Cross-correlation simulation of sequences with 20, 50 and 80 ns delay with 3 dB, 6 dB and 10 dB attenuation, respectively.

A FMCW signal was generated with properties which would achieve similar performance as a PN sequence would (in terms of maximum range, spatial resolution). The simulated correlation result with the original PN sequence is presented in Fig. 17.

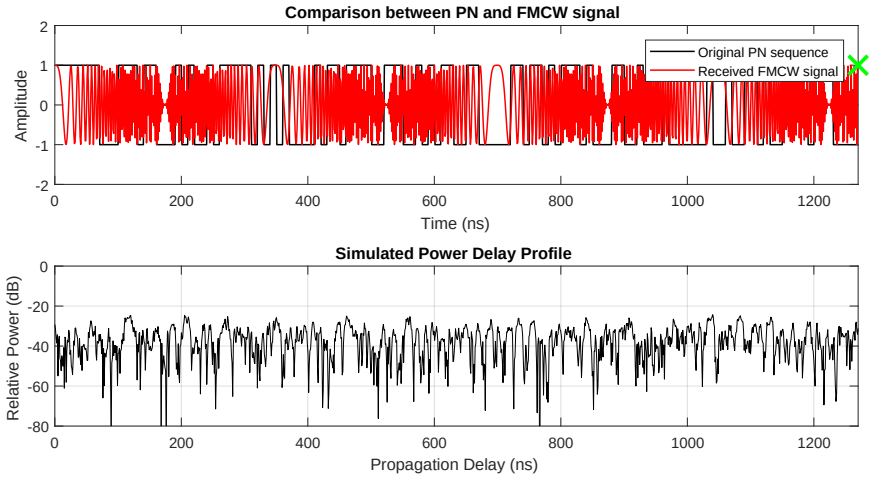

Figure 17: Cross-correlation simulation of a PN sequence with a FMCW signal.

Unlike the cross-correlation of identical PN sequences, the correlation of a PN sequence with an FMCW signal produces no clear correlation peak, where values only reach -25 dB, in this case.

Finally, the FMCW signal was then added to the previously generated multiple PN sequences to recreate a scenario where interference from nearby radars would occur.

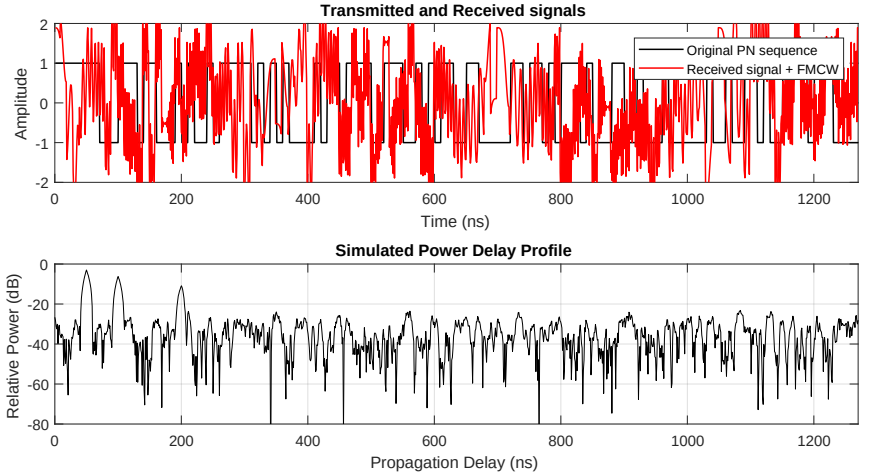

Figure 18: Cross-correlation simulation of a PN sequence with a FMCW signal and multiple PN sequences.

Fig. 18 depicts the effect of an FMCW signal interfering with multiple PN sequences. The correlation peaks are still clearly visible at their correct locations, where the resulting interference from the FMCW signal is once again located below -25 dB. This confirms that the STDCC technique between PN sequences are resilient

against FMCW signals transmitted by other radars, where the detected peaks are unaffected.

3.2 INTERIM CONCLUSIONS

This chapter presented the theoretical background behind the STDCC principle, by explaining the generation process of a PN sequence and the cross-correlation properties of such sequences. The method of obtaining the PDP of a channel is presented, which provides the received power and delay of each multipath component. Finally, the presence of an FMCW signal is studied, considering a scenario where both types of radar coexist and are transmitting at the same time.

This page is intentionally left blank.

4

IMPLEMENTATION OF A STDCC RADAR

This chapter will explain how the sounder was firstly implemented by the previous author in its initial state. After a brief study of the system, the steps taken to transition the channel sounder into a monostatic radar topology will be presented.

4.1 CHANNEL SOUNDER

The existing channel sounder, originally presented in [7], consists of two major blocks: the transmitter block and the receiver block represented in Fig. 19 and Fig. 20, respectively.

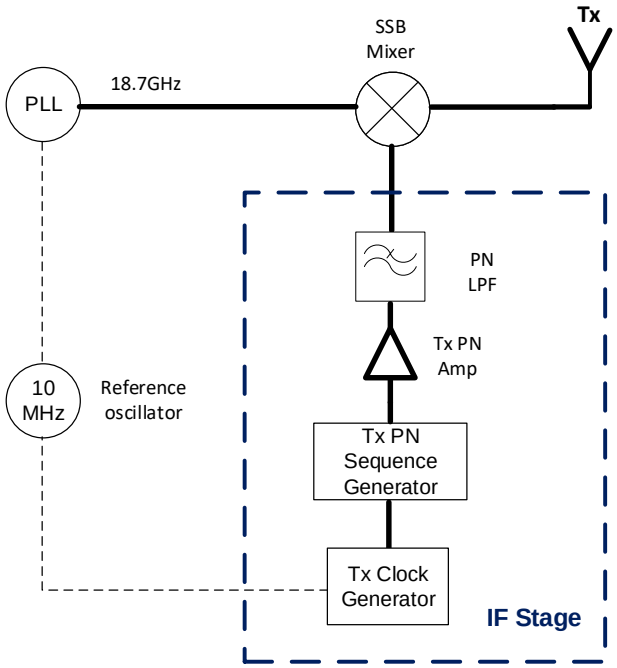

Figure 19: Channel sounder transmitter block diagram

4.1.1 *Sequence generation*

The clock signal governing the sequence generation is provided by a frequency synthesiser, namely the RF2052 evaluation board from RFMD. This synthesiser can operate from 30 MHz to 2.5 GHz with a resolution of 0.596 Hz (when a 10 MHz external reference is used) and a phase noise of -90 dBc/Hz at 10 kHz [28]. This

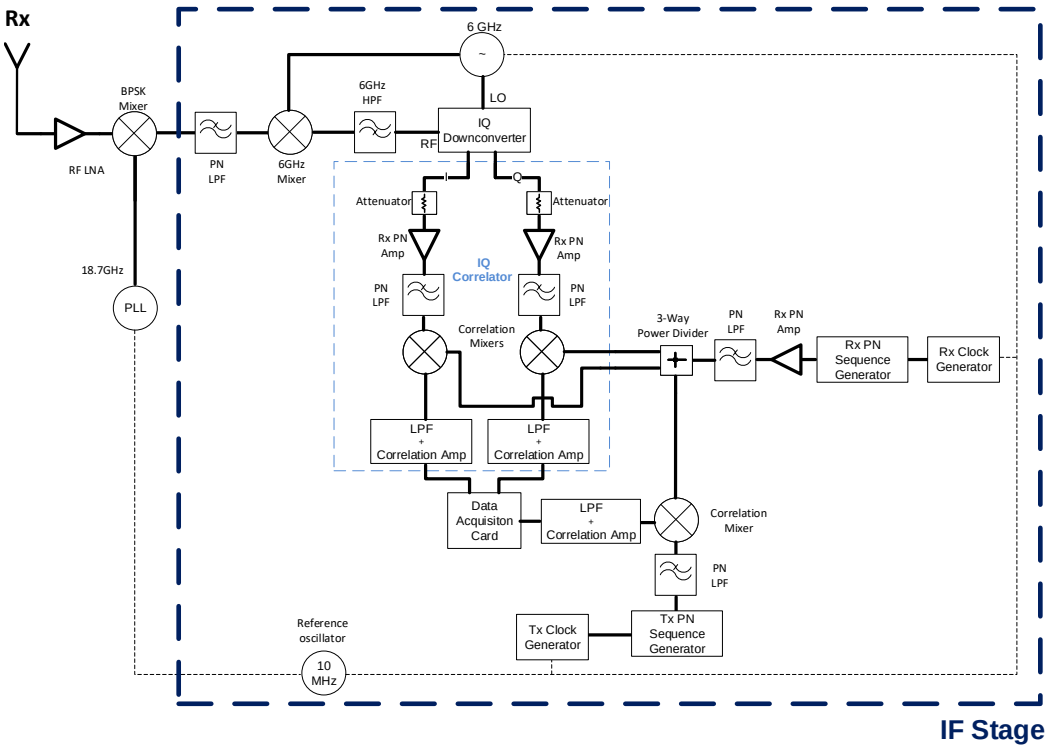

Figure 20: Channel sounder receiver block diagram.

device can be controlled by a proprietary computer software called *RFMD Slice Programming Tool*, where numerous settings can be changed and applied on the fly. As such, Fig. 21 depicts the output of the device, which was programmed to transmit a 2 GHz tone, reaching -10 dBm of output power. As for the 10 MHz clock reference, a PRS10 rubidium frequency standard was connected to the frequency synthesiser for its high stability (phase noise below -130 dBc/Hz at 10 Hz) [29].

A high throughput data transmission card, the Data Pattern Generator 2 (DPG2) from Analog Devices, was used to generate the desired PN sequences. The DPG2 is specifically designed to test Analog Devices' Digital-to-Analog Conveter (DAC)s, as it stores data vectors in its internal memory to then transfer said data through a Low-Voltage Differential Signaling (LVDS) connection with rates of up to 1.25 Gbps [30].

The conversion of this data to an analogue signal is accomplished with a AD9739-R2-EBZ Evaluation Kit, a 14-bit RF DAC. This device has a maximum conversion rate of 2.5 GSPS, low noise and intermodulation distortion for synthesising high quality signals up to 1 GHz [31].

After the sequences are generated, signal conditioning is necessary to comply with the input requirements of the RF mixers, by means of amplification and filtering. A Miteq AM-1607-2000 amplifier was used, having a 42 dB gain over a frequency range of 0.01 MHz to 2 GHz, a 1 dB compression point at 11.4 dBm and a noise factor of around 3.5 dB [32]. The Mini-Circuits SLP-1200+ was chosen as a simple low pass filter with a pass band frequency range from DC to 1 GHz and 3 dB cut-off

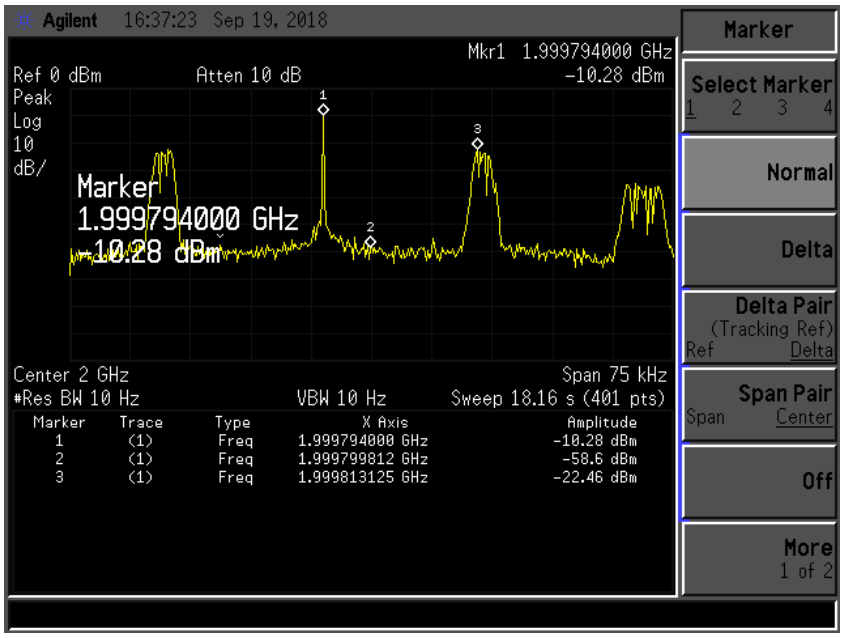

Figure 21: Spectrum of a 2 GHz signal generated by the RF2052.

frequency of 1.2 GHz [33] to filter out possible harmonic spurs originated by the sequence generation. The spectrum of the resulting PN sequence after amplification and filtering can be seen in Fig. 22.

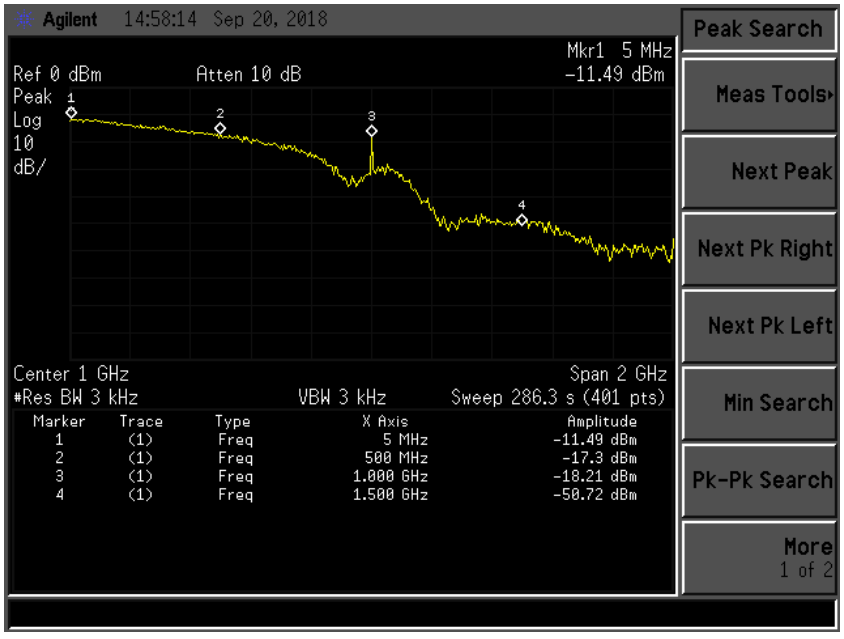

Figure 22: Spectrum of a 1 GHz PN sequence after after amplification and filtering.

4.1.2 *RF stage*

As previously stated, the sounder is designed to be highly flexible in regards to RF stage interchangeability, allowing the use of existing RF front-ends previously

developed. Nevertheless, these front-ends all function very similarly, where the input signal is up-converted with a mixer fed by a Phase Locked Loop (PLL) clocked at the desired frequency to then be transmitted via a horn antenna.

The RF front-end used for this project, depicted in Fig. 23 consist of an RF mixer, fed by an 18.6 GHz PLL to up-convert the sequence. The signal is then transmitted through a directional horn antenna into the channel. The inverse process is preformed in the receiver block in addition to employing a Low Noise Amplifier (LNA) before the down-conversion back to baseband.

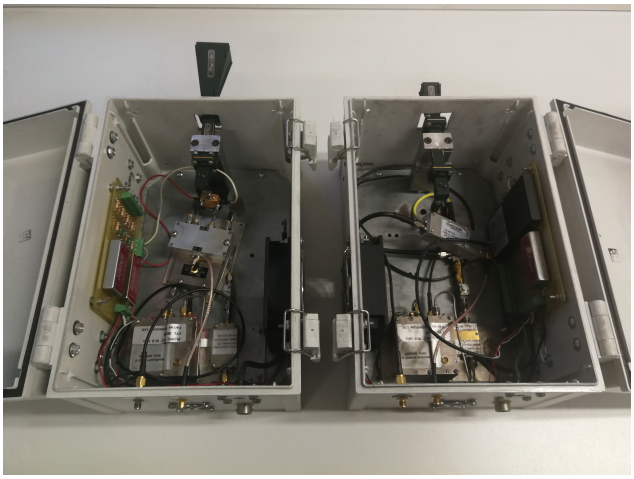

Figure 23: TX (left) and RX (right) RF front-ends at 18.6 GHz.

4.1.3 *6 GHz intermediate stage*

In the receiver block, the signal must first be up-converted to an Intermediate Frequency (IF) of 6 GHz to comply with the specifications of the IQ downconverter. A DLCRO-010-06000-3-12P from Miteq was chosen as a PLL, having an output power of 13 dBm; harmonic and spurious signals at -50 dBc and -70 dBc, respectively; and a phase noise of -110 dBc/Hz at 1 kHz. The 6 GHz mixer is a DM0408LW2, also from Miteq, which operates from 4 GHz to 8 GHz on the RF/Local Oscillator (LO) port and from DC to 2 GHz on the IF port. There is a typical conversion loss of around 5 dB and a minimum of 30 dB isolation between ports [34]. To mitigate possible IF to RF leaking, a VHF-4600+ high pass filter was used, with an operating frequency between 5 GHz to 11 GHz and a cut-off frequency of 4.6 GHz [35].

The IQ demodulator is a HMC-C009 from Analog Devices, having an operating frequency band between 4 GHz to 8.5 GHz on the RF and LO ports, hence the need to up-convert the received signal from the RF front-end. It has a conversion loss of typically 7.5 dB; LO to RF isolation of at least 30 dB; LO to IF isolation of at least 14 dB; an amplitude balance of 0.3 dB; and phase balance of 8° [36].

4.1.4 *Sequence correlation*

After demodulation into I and Q components, these signals are also amplified and filtered, similarly to the transmitter block, with AM-1469-2000 amplifiers from Miteq. These amplifiers have very similar characteristics than the AM-1607-2000, having a lower gain but higher 1 dB compression point [37].

With this, the received sequences are ready to be correlated with the sequence generated in the receiver block. A ZFM-2-S+ mixer is used for its operating frequencies: the RF and LO ports operate from 1 MHz to 1 GHz, while the IF port operates from DC to 1 GHz. The mixer has a conversion loss of 5.7 dB, LO to RF isolation of at least 25 dB and LO to IF isolation of at least 20 dB [38]. These characteristics are needed to allow the correlation of two distinct PN sequences (which occupy a bandwidth from DC to 1 GHz). The result of the correlation is a signal which presents low frequencies (in the order of Hz to a few kHz) and can be observed in Fig. 24.

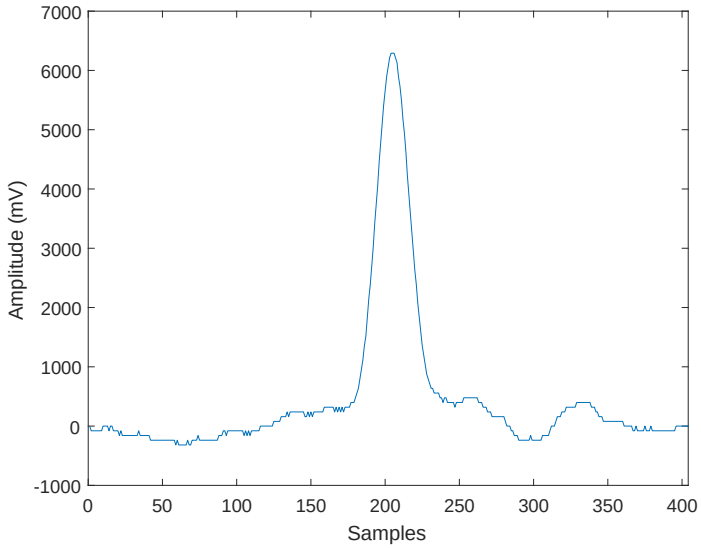

Figure 24: Correlation result between identical sequences.

The sequences generated in the receiver block are identical to the one generated in the transmitter block, with the exception of one of them having a clock signal with at a slightly lower frequency. The sequence generated with a frequency shift is to be correlated with 3 signals: the received signal from both I and Q branches and the second sequence generated in the receiver. The first 2 correlations will provide the channel information whilst the third will provide a correlation peak reference for data acquisition triggering.

The correlation result, as described in Chapter 3, consist of a low frequency signal, which needs to be amplified to an adequate level and filtered to then be acquired

by an Analog-to-Digital Conveter (ADC). A variable gain amplifier and variable low pass filter were developed by the previous user to provide flexibility depending on the scenario to be measured.

Finally, the data acquisition card used was a NI USB-6211 from National Instruments, having 16-bit resolution, 250k samples per second and a maximum range from -10 V to +10 V, capturing the data from each IF branch.

4.2 RECONFIGURATION TO RADAR

The proposed topology for the radar has the flexibility to be modified in a modular fashion, separating the sequence generation section, the RF front-ends, the 6 GHz down-conversion section, the correlation mixers and the data acquisition section. As such, modifications can be employed to improve each section independently, while maintaining the overall functionality of the system.

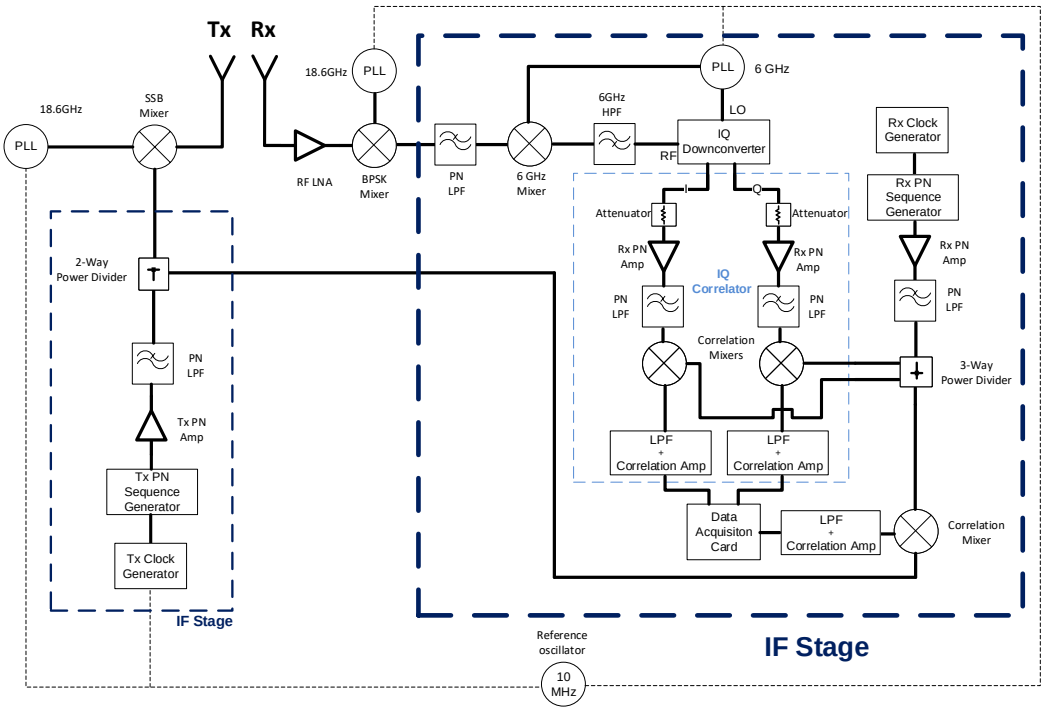

Figure 25: Radar block diagram.

By transitioning into a mono-static radar system, one of the first applied changes was to remove the duplicated sequence generator in the receiver block. As the transmitting and receiving antennas in the proposed radar topology coexist, the transmitting and receiving block can be located in close proximity, allowing the re-utilization of the sequence generator by employing a wideband splitter (ZFSC-2-2500 [39]). This change reduces the total volume and complexity of the system, sequence synchronisation shifts and possible errors while setting up, as one less sequence generator needs to be configured. This change can be observed in Fig. 25.

The RF front-ends were kept separate as to allow them to be used in other systems, although the possibility of using an RF circulator has been pondered to reduce the complexity of the system even further and mitigating possible RF oscillator frequency and phase shifts.

4.3 PRELIMINARY ASSESSMENT OF RADAR PERFORMANCE

A simple preliminary test was conducted in the laboratory to assess the initial performance of the channel sounder at the time. The TX PN sequence generator was clocked at 1 GHz and a slip rate of 100 kHz was defined by setting the RX PN sequence generator clock to 999.9 MHz. The sequence length used was 2047 chips (2^{11} - 1).

Firstly, back-to-back transmission was ensued, in order to view the correlation result of the sequence in each branch. A metallic pole with a diameter of 6 cm was placed 2 metres away from the RF front-ends antennas. The obtained result is shown in Fig. 26, where each point represents the maximum correlation value obtained for each PDP over time.

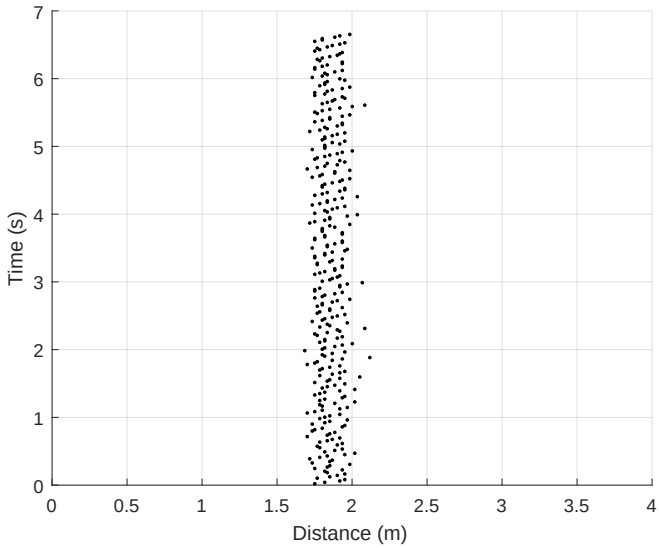

Figure 26: Radar preliminary test of a single metallic pole.

The obtained result depicts an object being calculated slightly under 2 metres, with a variation of around 30 cm. This variation is acceptable as it is within the spatial resolution parameter of the channel sounder using the mentioned PN sequence settings.

4.4 CALIBRATION INSIDE ANECHOIC CHAMBER

Further radar calibration was conducted inside a controlled environment, such as an anechoic chamber. Firstly the chamber's impulse response was measured when empty, followed by the introduction of one metallic pole which was placed at 2.5 m away from the radar antennas, as depicted in Fig. 27. Results presented in Fig. 28a depict the initial round trip time of about 17.5 ns due to direct (over-the-air) antenna coupling, acting herein as a time-reference for absolute time-delay measurements. This is due to the overall path time delay from initial TX PN sequence generator to the receiver frequency down-rated RX PN Sequence Generator, since the former is fed directly to the RX IF stage. The thickness of the line represents the system stability over time, which is mostly within the 2 ns time resolution, as expected. For simplicity, only the main correlation peaks will be presented in all graphs from now on.

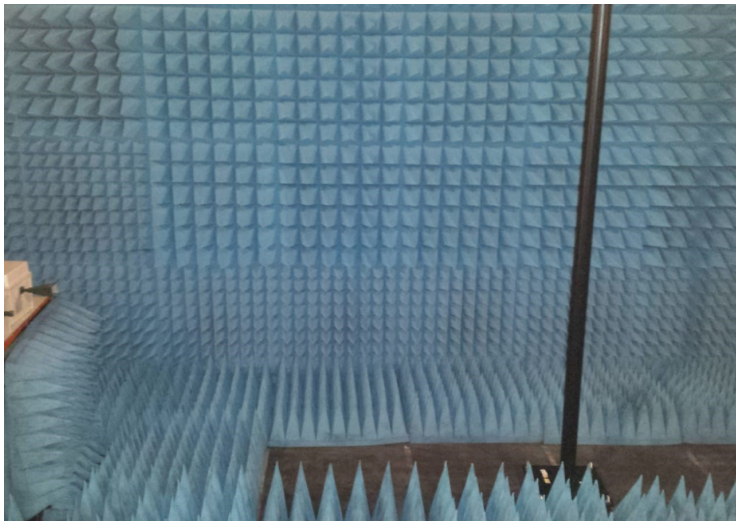

Figure 27: Anechoic chamber calibration setup.

By introducing the first metallic pole at 2.5 m away from the radar, one can clearly see the superposition of a second contribution, as depicted in Fig. 28b, followed by time normalisation to the direct antenna coupling, as presented in Fig. 28c. In the latter, yielded distances were computed, in which the displayed values of about 2.35 m can be extracted from the top horizontal axis (abscissa). This is in rather good agreement with the measurement geometry, clearly demonstrating the radar's accuracy in estimating the time-of-flight or distance to the object. The radar's radio system parameters are presented in Table 2.

These parameters consist of the gains and losses from the up-conversion mixer to the down-conversion mixer of the radio system, excluding path loss.

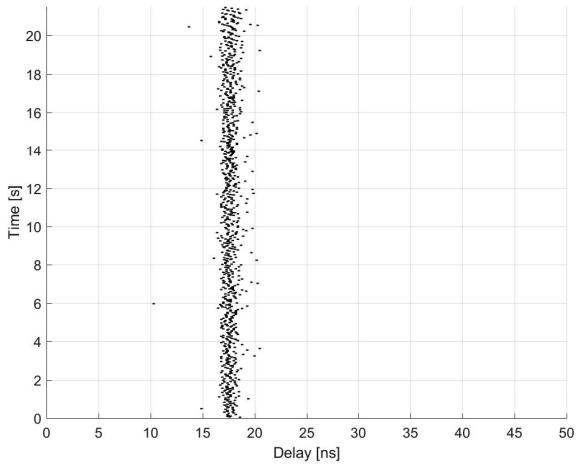

(a)

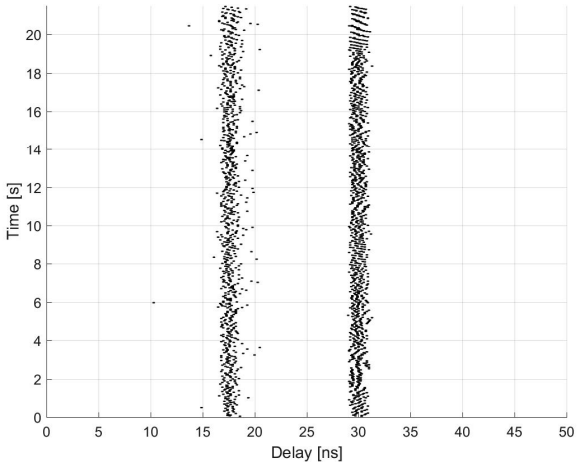

(b)

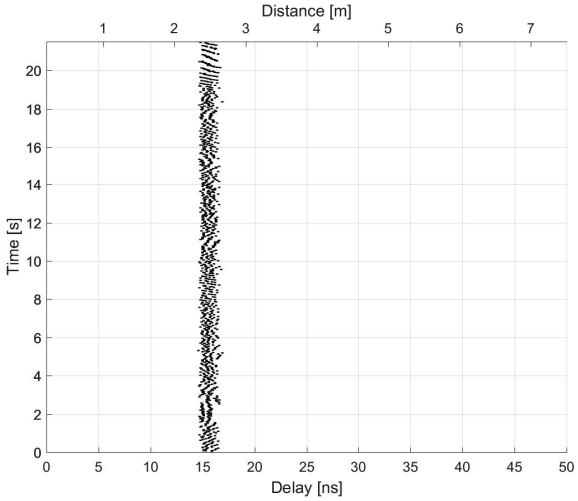

(c)

Figure 28: Radar calibration inside the anechoic chamber: (a) direct antennae coupling, (b) plus reflection from a single metallic pole, and (c) normalised reflection from the pole to the coupling component.

Parameter	Value
PN sequence power level	-19 dBm
PN to Tx mixer cable losses	2 dB
Tx mixer up-conversion losses	12 dB
Tx mixer to Tx antenna losses	1 dB
Tx antenna gain	20 dBi
Tx antenna -3 dB beam-width	23°
Rx antenna -3 dB beam-width	63°
Rx antenna gain	10 dB
Rx RF LNA amplifier gain	44 dB
Rx amplifier to Rx mixer losses	1 dB
Rx mixer down-conversion losses	10 dB

Table 2: Radio system parameters.

4.5 MOVING TARGET

To assess the moving target identification capabilities of the sounder, measurements were conducted with a moving target in the scene. Firstly, the radar's capability to detect the trajectory of a person was realised inside the anechoic chamber. A similar test was conducted in the group's laboratory, a highly dense cluttered environment.

4.5.1 *Controlled environment*

People moving detection trials have been made inside the anechoic chamber, where a person was made to appear in the scene and walk towards the metallic pole (placed in the centre of the anechoic chamber), walk beyond it and then back again towards the sounder and eventually disappear from the scene, always at a steady pace, as depicted in Fig. 29.

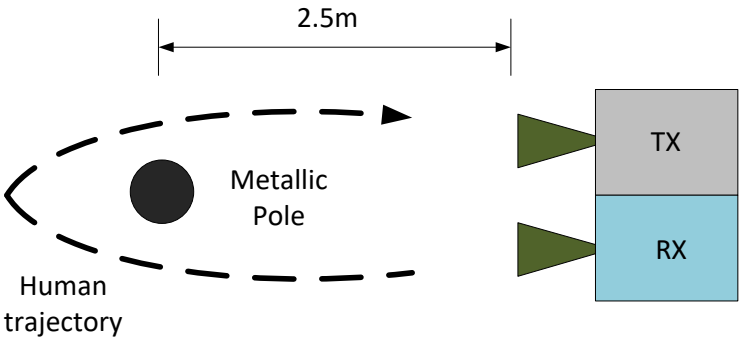

Figure 29: Moving target measurement setup.

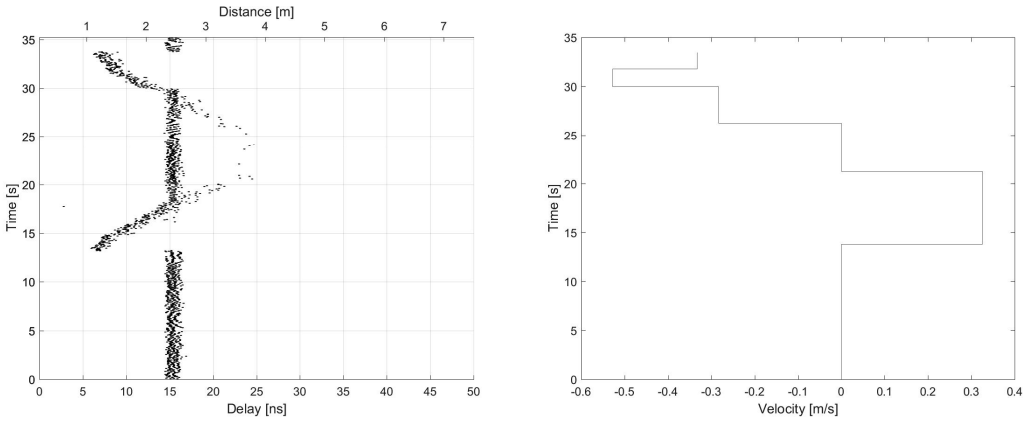

(a) (b)

Figure 30: Measurement results for the case of a forward and back moving person in the radio path between the sounder and a metallic pole, inside the anechoic chamber: (a) absolute time delay and distance; and (b) long-term averaged radial velocity evaluation

Results presented in Fig. 30a clearly picture out the moving target trajectory over time. From these, it is possible to infer the person's walking velocity by calculation of the instantaneous or long-term averaged radial velocity from first order derivation of the curve presented in Fig. 30b (top abscissa axis) over elapsed time (ordinate axis). And from this, the sense of motion can be obtained (being positive and negative slopes) when the target is moving away or towards the sounder, respectively.

4.5.2 *Highly dense clutter environment*

Finally, similar analysis was performed in a highly dense clutter environment such as the group's laboratory, as previously mentioned. Here the target was made to move in linear motion back and forth in a 1 to 3 m range in front of the sounder. The target consisted of a metallic plate with dimensions of 0.5 m by 0.5 m, yielding a RCS of -6 dBsm, confirmed from simple link budget analysis. The results are presented in Fig. 31.

Fig. 31a depicts all detected peaks within 10 dB from the maximum value, where one can identify long delay tails, corresponding to reflections from walls and furniture of reasonable amplitudes. For simplicity, only the correlation peaks were processed and thus a clean PDP over time is presented in Fig. 31b. The same velocity calculations performed in the previous measurement can be seen in Fig. 32.

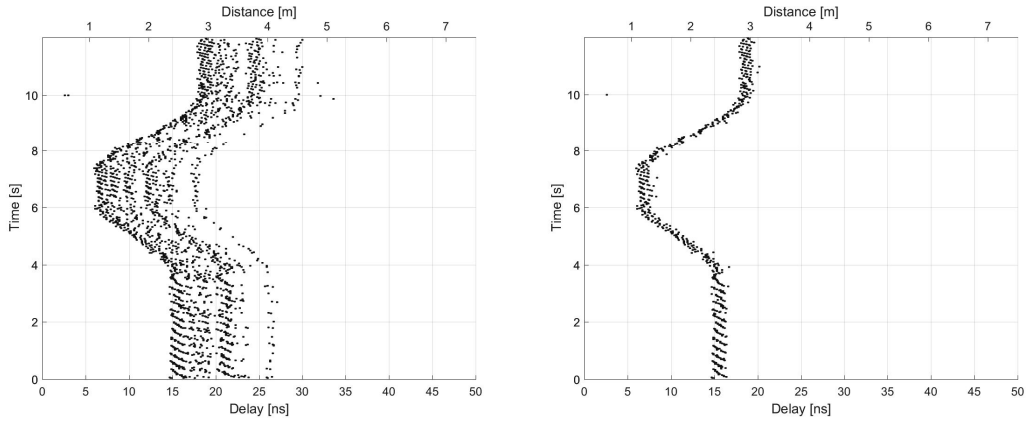

(a) (b)

Figure 31: Absolute time delay and distance of measurement result for the case of a forward and back moving metallic plate in a cluttered environment: (a) full result; and (b) maximum values.

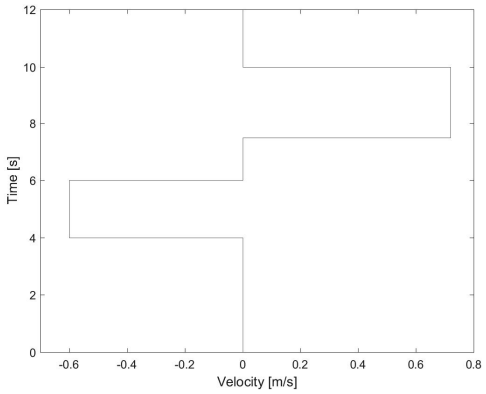

Figure 32: Long-term averaged radial velocity evaluation of measurement result for the case of a forward and back moving metallic plate in a cluttered environment

4.6 INTERIM CONCLUSIONS

These are sought to be initial results of the application of a highly scalable channel sounder to act as a monostatic radar. Notwithstanding the limitations and the simple measurement scenarios reported herein, the proof-of-concept of a complete real-time radar based on PN sequences is remarkably promising and provides the rationale to continue with further improvements.

5

RADAR IMPROVEMENTS

5.1 A NEW RF FRONTEND AT 24/28 GHZ

In order follow the aim of the RETIOT project to meet the recent 5G NR specifications, particularly in Europe, a new programmable RF frontend was designed to operate from 24 to 28 GHz. This allows the frontend to be used in other 5G NR applications while also operating within the standard 24 GHz radar frequency band. The RF frontend was built using the state-of-art "drop-in and drop-on" RF components from X-Microwave Innovative Modular Building Block System (X-MWblocks) [40].

5.1.1 *X-Microwave Building Block System*

Each block consists of the implementation of a single RF device, such a mixer, amplifier, oscillator, splitter, frequency multiplier, PLL and much more. X-MWblocks are sought to be easy to test, integrate, align and configure, from prototype to final production hardware. Each RF frontend occupies an area of 98 mm by 61 mm (excluding the antenna). Fig. 33 depicts both TX and RX frontends.

Figure 33: The complete 27 GHz RF Frontend using X-Microwave Innovative Modular Building Block System.

The TX block, presented in Fig. 34a, consists of an 80 MHz reference oscillator clock, feeding into a PLL frequency synthesizer capable of outputting an RF signal

from 54 MHz to 13.6 GHz. This signal is then filtered and amplified to conform to the input parameters of the frequency multiplier, which will originate a 27 GHz carrier signal to feed into the LO port of the RF mixer to up-convert the PN sequence generated in the IF stage. The PN sequence generation stage is identical to the previously presented system diagram. Finally, the modulated signal is amplified and transmitted through a directional horn antenna.

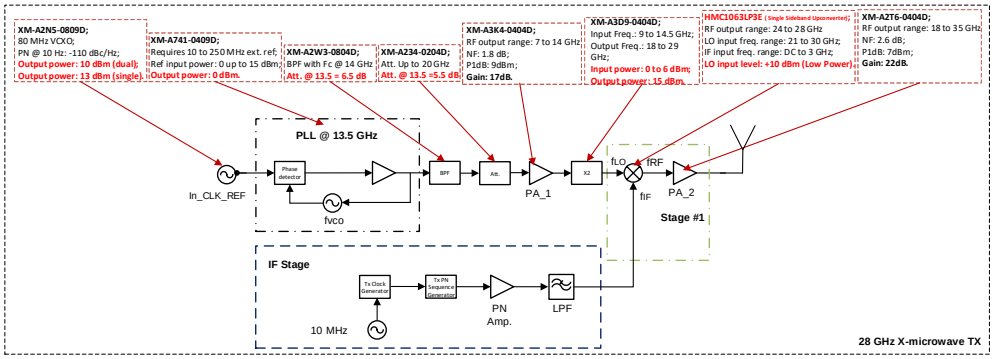

(a)

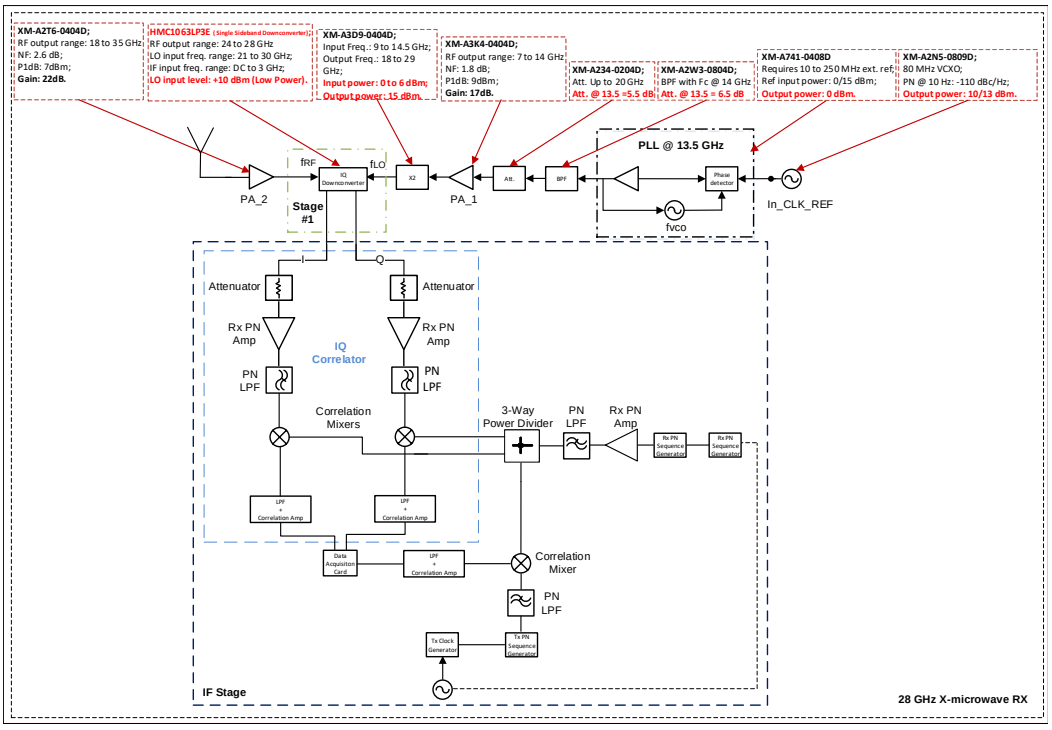

(b)

Figure 34: The complete 28 GHz channel sounder: (a) transmitter and (b) receiver block diagrams, respectively.

On the receiver end, the signal captured by the antenna is amplified and fed into an IQ RF mixer for down-conversion. Again, this allows us to receive I and Q components. The LO signal is generated identically as the one in the TX block.

5.1.2 *Calibration*

Calibration of the radar is necessary to convert the resulting correlation amplitude into the corresponding attenuation of the radio channel. This calibration has been performed by connecting the TX and RX blocks trough a variable attenuator. Values ranging from 0 dB to -90 dB of attenuation were set and the correlation result measured, providing the data for Fig. 35.

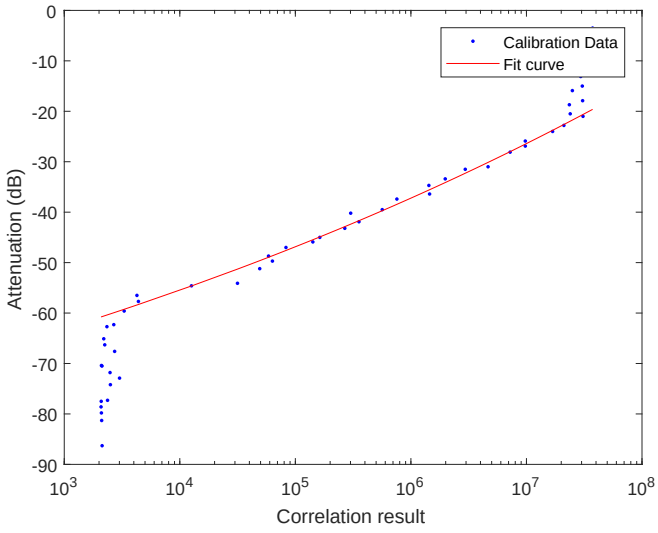

Figure 35: Relation between attenuation and correlation amplitude

A fitting curve was applied to the linear region of the data to extract a calibration equation to then be applied on the following measurements, allowing the conversion of received correlation amplitude to attenuation in the radio path.

5.1.3 *Measurement trials and results*

Propagation measurement trials in a Factories of the Future (FoF) use case scenario have been conducted using the new test rig, which includes real-time channel sounding and angle-of-arrival capabilities, as depicted in Fig. 36. The receiving antenna was placed at a height of 1.5 m on top of a miniature pan-and-tilt positioner and at a distance of 4 m from the transmitter, in an environment surrounded by Computer Numerical Control (CNC) machinery. A lens horn antenna of 1.8° of beamwidth and a gain of 33 dBi was employed at the receiver, while at the transmitter, a 20 dBi (19° of beamwidth) standard horn antenna was used.

Measurement results are presented in Fig. 37 for an azimuth angle scan from ±114°, in increments of 1°. For each azimuth angle of the receiver antenna, the PDP was measured, as shown in Fig. 37. From a close observation of the measurement results, it becomes clear that no significant Multipath Component (MPC) are present

in the radio path, being the direct component (line-of-sight) the only propagation mode. Even in azimuth angles well away from boresight, i.e. at around ±114°, no relevant MPC activity was detected.

Figure 36: 5G use case - factory of the future (or Industry 5G).

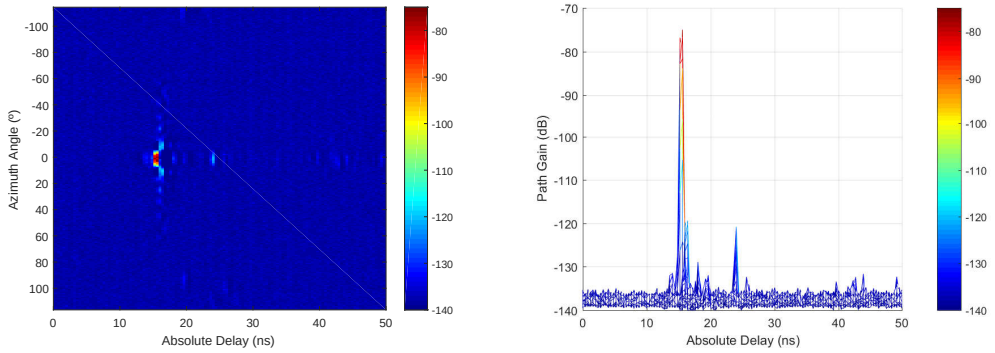

(a)

Figure 37: Measured power delay profile for all azimuth angles as a function of: (a) azimuth angle over absolute delay; and (b) absolute delay.

5.2 BASEBAND IMPROVEMENT BASED ON FPGA AND COMPARISON WITH COTS SOLUTIONS

5.2.1 *Radar Topology*

This section thoroughly details the proposed system giving the necessary technical insight about the radar architecture. For instance, Fig. 38 depicts the block diagram of the radar topology. The block diagram is divided in two sub-systems, corresponding to different stages of the system's architecture, namely the RF and IF stages.

In the RF stage, a high precision Voltage-controlled oscillator (VCO) is used to lock the PLL configured to output a 12.0 GHz RF signal. After appropriate signal conditioning (filtering and amplification) to suppress undesired spurious signals and adjust the power level, a frequency multiplier is employed to achieve the necessary

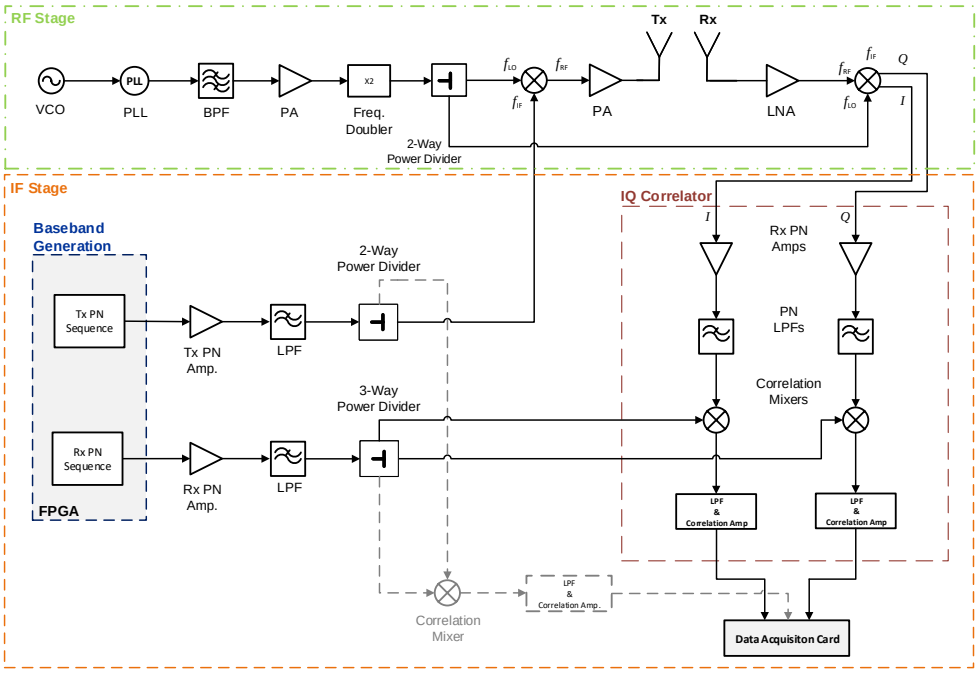

Figure 38: Block diagram of the STDCC radar architecture.

$f_{LO} = 24$ GHz reference signal. This, in turn, is used to source both the Single Side Band (SSB) up-converter and the IQ down-converter mixers using a 2-way power divider. Thus, the Tx mixer up-converts the base-band signal (f_{IF}) generated by an FPGA (Tx PN Sequence) in the IF stage block into a 24 GHz RF signal. Subsequently, an amplification stage is considered to increase the output power level up to the limits of interest for the radar. On the other hand, the Rx mixer de-modulates the RF signal from the radio channel that contains radar information, into a differential signal with I and Q components that inputs the IQ Correlator in the IF block.

The RF stage (Fig. 38) is implemented using *X-Microwave* technology, which is a complete modular building block eco-system for microwave components that allow easy integration of RF components, aiming at fast prototyping. Two identical 20 dBi standard gain horn antennas (*Flann* 22240-20) are used side-by-side, as transmitter and receiver, distanced 1 cm apart.

In the IF Stage, a 511 bits length pseudo-noise sequence of MLSR type is generated by an FPGA at two different rates. The sequence to be transmitted over-the-air (Tx PN sequence) has a sampling rate of $f_{seqTx} = 250.1$ MHz whereas the one to be correlated in the receiver (Rx PN sequence) is decreased by 100 kHz, resulting in a sliding factor of $k = 2500$ according to (13) [7, 27]. Specifics about the baseband PN sequence generation are detailed in Section 5.2.2.

$$k = \frac{f_{seqTx}}{\text{slip rate}} = \frac{f_{seqTx}}{f_{seqTx} - f_{seqRx}} = 2500 \tag{13}$$

The differential signal that is fed into the IQ Correlator block and contains the radar information is amplified and filtered before being correlated with the Rx PN Sequence generated by the FPGA. The I and Q signals are analysed in both independent branches allowing for *Doppler* detection.

After correlation, the resulting signal is amplified and filtered, in order to be properly detected by a Data aquisition (DAQ) card. To this extent, specific electronic circuitry was developed, comprising two printed-circuit boards for the amplifier and filter components, respectively. A 12-pole switch was included so that pre-defined gains can be adjusted according the specific dynamic range envisaged for a specific geometry/measurement. The gain of the post-correlation IQ signals can vary from 14 up to 19 dB, providing an appropriate level for the DAQ card input ports. As per the low-pass filter, a 7^{th} order *Chebyshev* filter, with maximum theoretical ripple of 0.01 dB, and a cut-off frequency of 200 kHz (twice the slip-rate), was implemented. This type of filter was chosen due to its steep roll-off, while minimising the pass-band ripple.

The acquisition of the correlation signals is done using a ordinary DAQ, i.e. *Picoscope* 3406-D MSO, with 4 analogue inputs of 250 MHz bandwidth, and a maximum sampling frequency of 1 GS/s and 8 bits of resolution.

In order to obtain a clear temporal reference, an optional auto-correlation stage could be included (as marked in grey colour in Fig. 38), at the expense of using one extra correlation mixer, amplifier and filter. This is currently used in the system to reference the temporal instants and to trigger the data acquisition card for signal measurement.

5.2.2 *All-Digital Baseband*

The baseband block, marked with blue-dashed line in Fig. 38, is the radar sub-system responsible for generating the receiver and transmitter PN sequences. This implementation adopts 511 points maximum length real-valued bipolar PN binary sequences. The real-valued bipolar PN binary sequences open way to the use of the FPGA's unipolar digital output pins, followed by a DC removing block, to generate the analogue baseband signal, thus eliminating the need to use expensive high-speed DAC converters. The block diagram of this sub-system is depicted with more detail in Fig. 39. The baseband is composed of 3 main blocks: Clock generation, Transmitter Sequence Generation and Receiver Sequence Generation. Its outputs feed both IF stage PN amplifiers identified in Fig. 38.

The clock generation block outputs 2 digital clock signals with frequencies of 250.1 MHz and 250 MHz that feed, respectively, the transmitter sequence gen-

eration and receiver sequence generation blocks. The different frequencies fed to the transmitter and receiver sequence generation blocks are responsible for the previously identified sliding factor, crucial for the operation of the STDCC [7,27,41] algorithm. To generate two clock signals at close but different frequencies, from a single reference clock signal with a frequency of 125 MHz, two reconfigurable PLL blocks (RX Clk Generator and TX Clk Generator in Fig. 39) must be used inside the FPGA. Because this circuit was implemented in a Xilinx Kintex-7 FPGA KC705 Evaluation Kit [42], the PLL blocks are implemented with 2 Xilinx's Mixed-Mode Clock Manager (MMCM) [43]. The receiver MMCM receives the 125 MHz clock signal and is configured to output 2 clock signals with different frequencies: the 250 MHz clock signal that will drive the receiver sequence generation block, and a 13.864818 MHz clock signal that will drive the transmitter MMCM. The transmitter MMCM is configured to output the 250.1 MHz clock signal that will drive the transmitter sequence generation block.

The transmitter and receiver sequence generation blocks are identical. The only difference is the frequency of the clock signal that drives them. Each sequence generation block is composed of a binary counter and a Read-Only Memory (ROM). The 9-bit binary counter counts from 0 to 510, sequentially addressing the 512-words, single bit-depth ROM. The ROM holds the unipolar version of PN binary sequence adopted in the implementation. The outputs of both ROMs are routed to 2 digital output pins, configured with the highest slew rate and drive strength.

5.2.3 *Practical Implementation and Performance Analysis*

In order to assess the performance of the proposed radar, a measurement setup was assembled inside the anechoic chamber to reduce the multipath effects and avoid possible external RF interferences. The radar prototype was placed at the centre of the 6 m by 5 m chamber, as shown in Fig. 40, on top of a motorised turntable, that enables 360° rotation in the azimuth plane (represented herein by θ) with

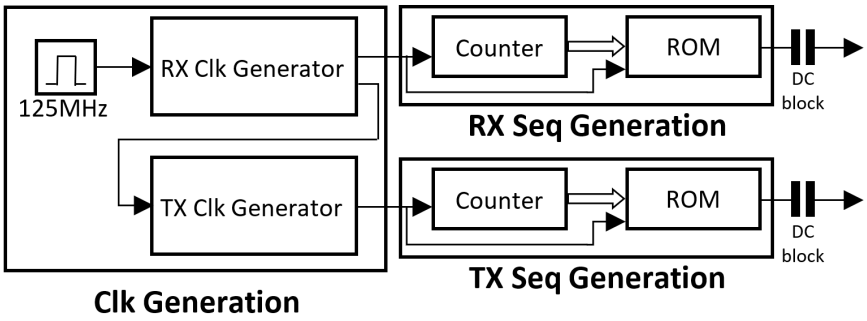

Figure 39: STDCC radar baseband.

0.5° resolution. Several case studies have been considered by placing metallic poles with 6 cm of diameter and 2 meters height, at the vicinity of the radar.

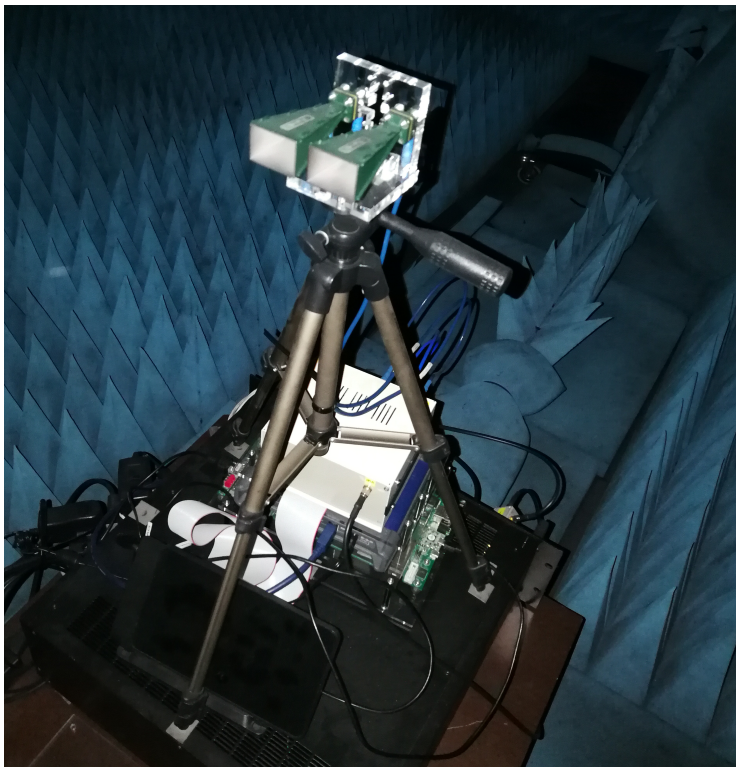

Figure 40: Photography of the STDCC radar prototype.

The poles were distributed inside the anechoic chamber according to the geometry depicted in Fig. 41. Radar measurements for distance and angular dependences have been performed in the following order:

1. 7 metallic poles, placed at alternating distances of 1 m and 2 m apart of the proposed radar aperture, in increments of 45°, as shown in Fig. 41a;
2. 8 metallic poles, 7 placed at 2 m apart of the proposed radar aperture, in increments of 45° and one pole placed at 1 m at boresight direction, as Fig. 41b depicts.

For both geometries, the radar system under test was made to rotate 360° with a 0.5° step increment.

As explained previously, both I and Q signals were considered for correlation and their results have been squared and summed together which, when plotted, yield the PDP result per angle. To better illustrate the performances of the radars, the results are plotted in two graph types: waterfall plot and polar plot, as depicted in Figs. 42a and 42b, respectively. While the waterfall graph presents the measured averaged PDP, for every angular step in the azimuth plane, displaying the radar distance in the y-axis and the azimuth angle in the x-axis, the polar plot shows

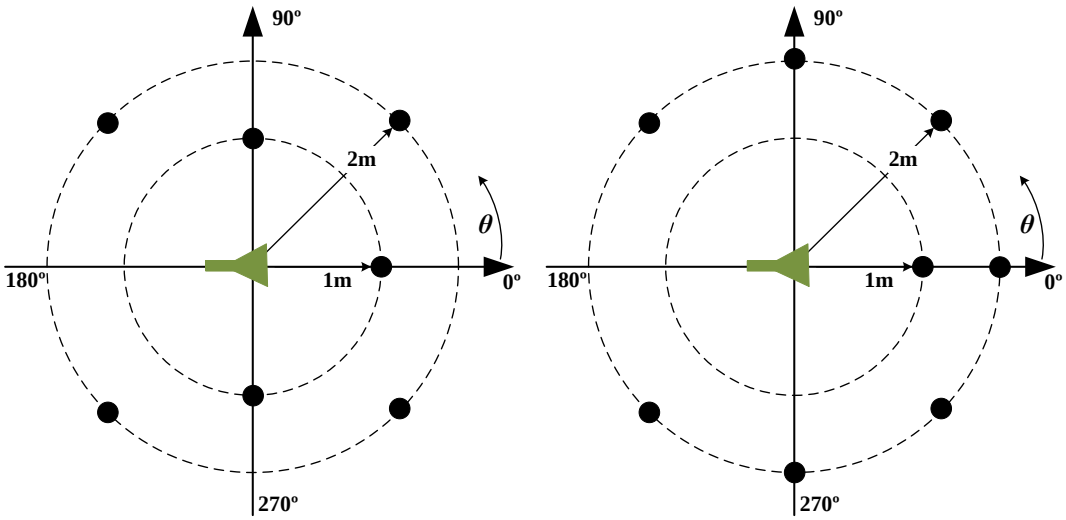

(a) (b)

Figure 41: (a) Radar 360° setup with 7 poles, (b) Radar 360° setup with 8 poles

the detected peaks, at each scanned angle, after running a simple peak-detection algorithm.

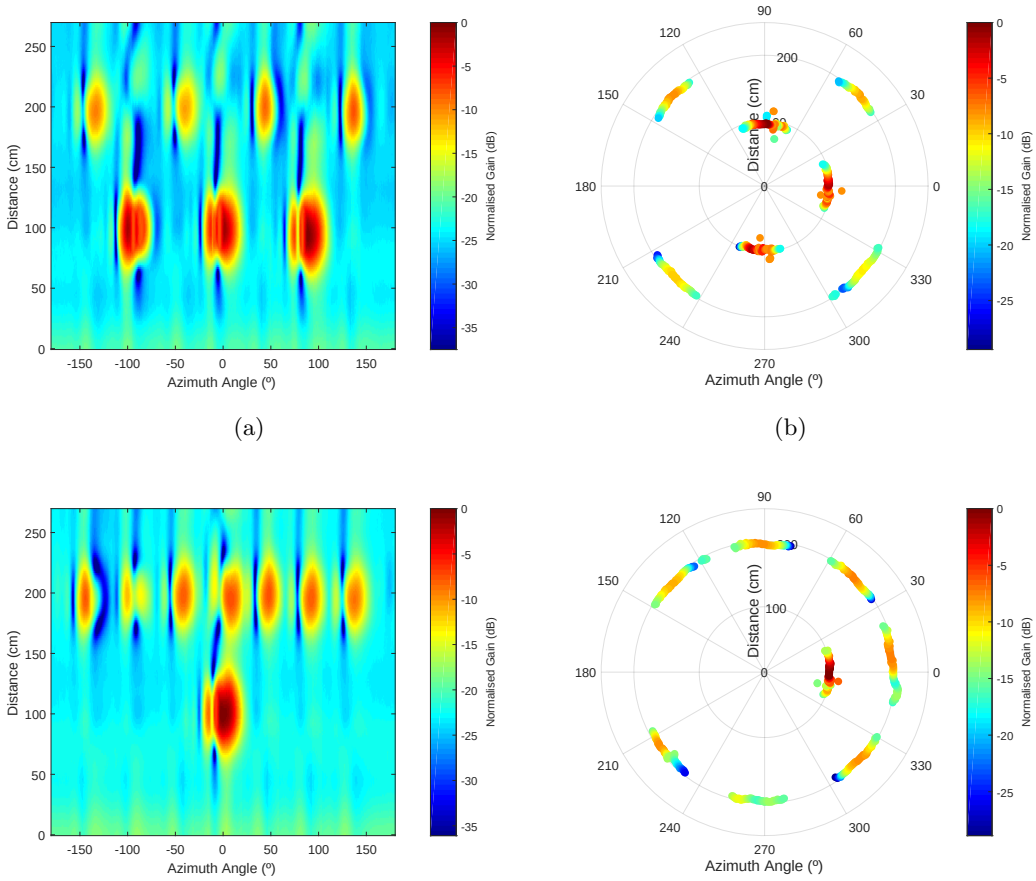

(a) (b)

(c) (d)

Figure 42: Experimental results for multiple poles scenario: (a, c) waterfall PPI plots and (b, d) polar PPI plots for the 7 poles setup and 8 poles setup, respectively.

From Fig. 42a it can be seen that all 7 poles of the first scenario are being detected correctly at 1 m and 2 m away from the radar in an alternating fashion. Fig. 42b confirms that these poles are being detected at the angles of -135°, -90°, -45°, 0°, 45°, 90° and 135°. On the second scenario, all poles are also correctly detected, where 7 are located at 2 m apart from the radar at the same angles as the previous scenario and a single pole placed at 1 m apart at the angle $\theta = 0°$. Most notably, the pole at also $\theta = 0°$ and 2 m further away is also being detected, while direct line of sight is not available. Although the angle of this pole is being detected as being at around 7° in Fig. 42d due to the *shadowing* of the pole at 1 m, the remaining poles seem to be detected at their correct angles.

5.2.4 *Comparison with commercial FMCW radar*

To compare the performance of the proposed STDCC radar with an off-the-shelf FMCW commercial solution (Distance2Go, from Infineon), another set of measurements were considered, focusing on resolution and the capabilities of discerning targets in close proximity. As such, the following measurements have been conducted:

1. A single metallic pole, placed 1 m apart of the proposed radar aperture, at boresight direction ($\theta = 0°$);
2. Two metallic poles, one placed at 1 m at boresight direction and the other at 1.6 m steered off 10° from the boresight direction ($\theta = 10°$).

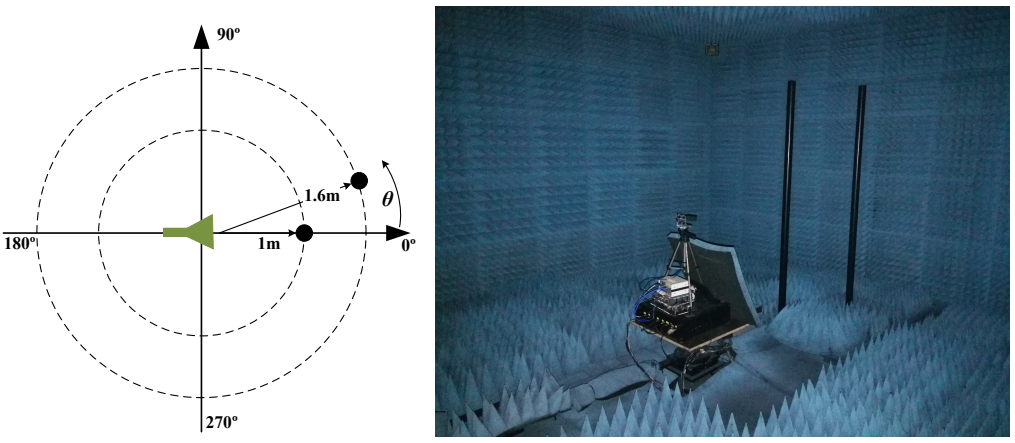

(a) (b)

Figure 43: (a) Radar benchmark setup, (b) Two-pole experimental setup assembled inside the anechoic chamber.

It is important to mention that for every step taken, 20 radar acquisitions have been measured and then averaged (PDP) to obtain a Plan Position Indicator (PPI) and assess the target identification performance on both systems.

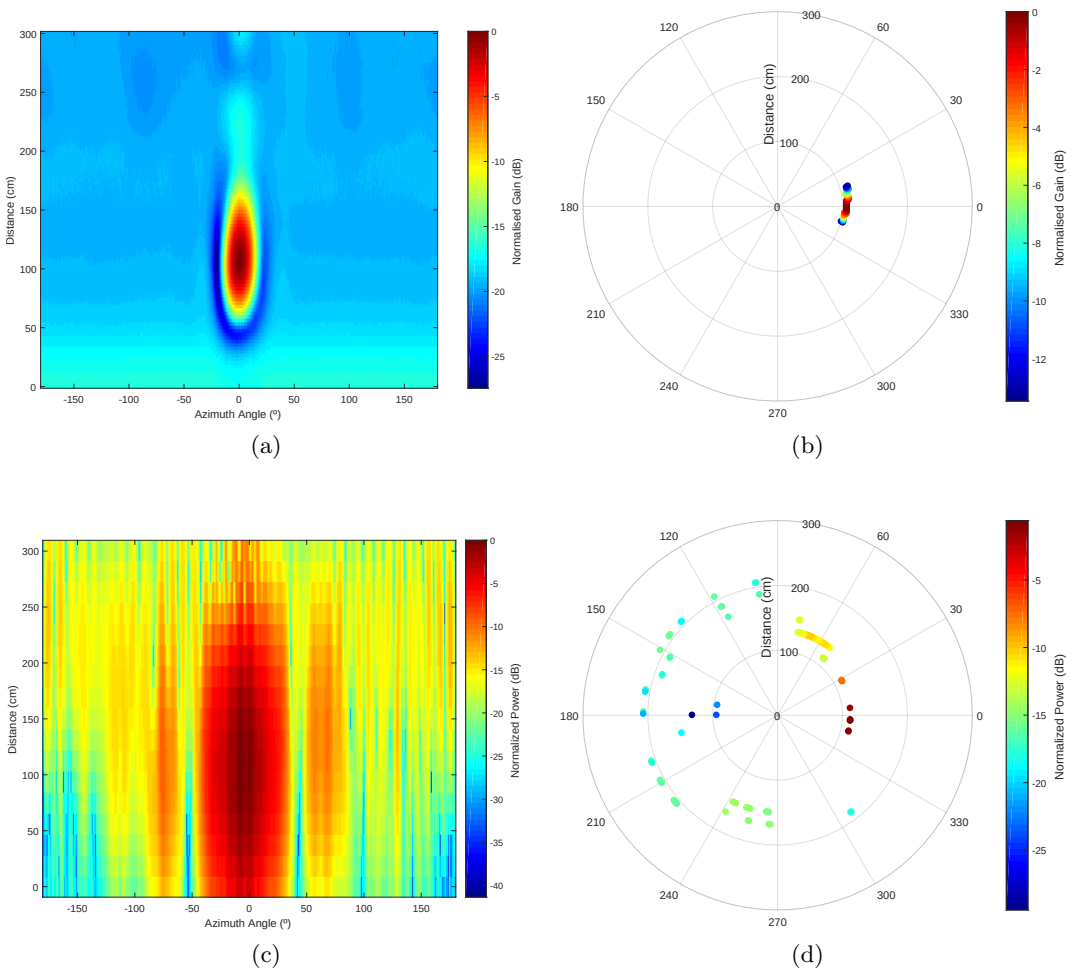

Figure 44: Experimental results for one-pole scenario: (a, c) waterfall PPI plots and (b, d) polar PPI plots for, the STDCC and FMCW radars, respectively.

From Fig. 44a, it can be concluded that the STDCC radar is accurately detecting a peak at 1 m distance at 0°, corresponding to the correct pole location inside the anechoic chamber. In fact, this can be confirmed in the plot of Fig. 44b, that clearly identifies an object at 1 m away from the radar at boresight direction to the object. However, it is worth to mention that the gradient variation of colours around the detected object, in Fig. 44a, is associated to the antennae radiation pattern discrimination that exhibits an half-power beam-width of around 23°, in both azimuth and elevation planes, at the considered frequency.

On the other hand, with the commercially available radar, it is also possible to detect the same pole, as depicted in the PPI of Fig. 44c. From the experimental data, an object is detected at 0° and a peak value at 1.1 m. Interestingly, several artefacts, albeit being 5-10 dB below the main contribution, are also observed almost in any direction. Due to this fact, the polar plot of Fig. 44d depicts false positives, since other peaks rather than the main contribution have also been detected by the peak-detection algorithm.

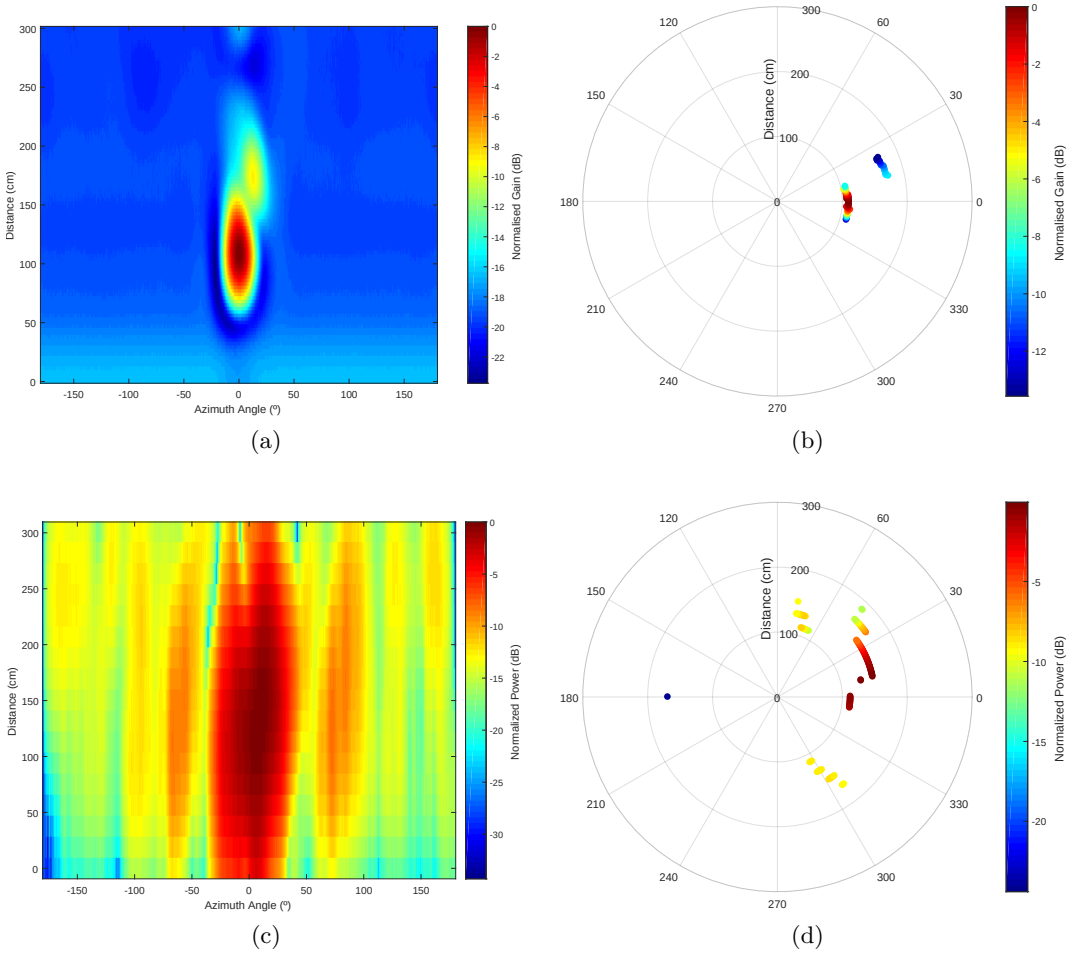

Figure 45: Experimental results for two-pole scenario: (a, c) waterfall PPI plots and (b, d) polar PPI plots, for the STDCC and FMCW radars, respectively.

Furthermore, when maintaining the 1 m distance pole and adding a second pole at 1.6 m deviated 10° in azimuth (according to the diagram of Fig. 43a), it is possible to observe that both radars are detecting the artificial targets. From the experimental results of Fig. 45, both STDCC and FMCW radars are still able to detect the metallic pole placed 1 m distance, with the STDCC radar (Fig. 45a) presenting a slight advantage with a greater measurement accuracy, when compared with the FMCW one (Fig. 45c). However, when the second pole is added to the scenario, it can be seen from Fig. 45c that the commercial solution fails to resolve such object. Although a slight increase in power at the region of $\theta = 10°$, d = 1.5 m is noticed, it is not possible to clearly distinguish between the two objects. In fact, it seems the second pole is masked by the effect caused by the pole placed at 1 m apart. Similarly to the first measurement (Fig. 44c), many artefacts are also observed in the 360° scan with amplitudes 5-10 dB below the main reflections.

In this particular case, the STDCC radar really show its merits and stands out from its counterpart, since it is able to clearly detect and distinguish both metallic poles (Figs. 45a and 45b), at the correct locations, *i.e.* first pole at $\theta = 0°$, d = 1 m

and second pole at $\theta = 10°$, d = 1.6 m. In fact, these results have been consistent throughout a series of repeated measurements, and a maximum range discrepancy of only 9 cm has been detected between experimental radar data and effective physical distance. This error is acceptable, as it falls within the spatial precision associated with the bandwidth used in the proposed radar. The signal level difference of about 7-9 dB observed in Fig. 45a is due to the excess path loss corresponding to distance of flight between poles (i.e. 1.2 m), in addition reflection loss introduced by the second pole (i.e around 2 dB).

5.3 INTERIM CONCLUSIONS

A complete baseband sequence generation migration to an FPGA based system has been implemented and tested against a commercially available radar solution. From the results above, it is possible to state that the proposed system is capable to detect closely spaced objects in the limit of the radar spatial resolution and thus presenting a remarkable performance over the tested commercial solution.

This page is intentionally left blank.

6

CONCLUSION

6.1 SUMMARY OF RESULTS

The main focus of this dissertation aimed at improving upon the already existing channel sounder in the investigation group at IT - Leiria. As such, channel sounding techniques were studied to better understand the existing system. After initial measurements of the channel sounder, a new RF frontend was developed and implemented at 28 GHz to follow 5G NR specifications. Measurements in a 5G NR factory scenario confirmed the high dynamic range of the system of around 60 dB. The baseband PN sequence generation stage was also improved by employing an FPGA. Measurement trials were carried out to evaluate the angular performance of the radar in a 360° scenario and all targets were successfully detected. The spacial resolution of the proposed system was observed to be around 60 cm, presenting a better performance when comparing with a COTS radar solution.

In Chapter 1, a brief introduction and background information of this dissertation is presented, as well as summarising the contents of each chapter.

Chapter 2 provided an explanation on the radar principle and the characterization of radio channels. Various channel sounding methods are studied, including existing systems found in the literature.

The contents of Chapter 3 focus on explaining the STDCC principle and its foundations. It is shown how a PDP is obtained for the extraction of the necessary information about a radio channel. The auto-correlation properties of PN sequences in regards to being resilient to the commonly used FMCW radar signals was also explored.

In Chapter 4, the initial state of the existing channel sounder was presented, explaining the function of each component in the system and its operation. A calibration was performed inside a controlled environment and initial measurements were made with static and moving targets.

Chapter 5 introduces the improvements made to the radar, such as the new RF frontend and baseband migration to an FPGA based solution. Measurements were conducted following these improvements, ultimately comparing them with a COTS

solution. The implemented system was capable of detecting closely spaced objects within the radar spatial resolution limits.

6.2 PUBLISHED WORKS

The research work carried out in this dissertation has been published in various international conferences, containing most of the work performed in this dissertation.

Papers in conferences:

- A. Sardo, B. Tribovane, H. Gomes, R. F. S. Caldeirinha, **"See-through wall imaging and motion detection using an ultra-wideband real-time RADAR at 18 GHz: first results"**, *Loughborough Antennas & Propagation Conference - LAPC*, Loughborough, United Kingdom, November, 2018;
- R. F. S. Caldeirinha, N. Leonor, A. Sardo, C. Ribeiro, G. Ramos, **"Radio Channel Sounder for 5G Propagation Modelling at 28 GHz - Initial Trials on the Factory of the Future Use Case"**, *Conference on Telecommunications - ConfTele*, Lisbon, Portugal, June, 2019;
- R. F. S. Caldeirinha, J. R. Reis, A. Sardo, L. Duarte, N. Leonor, J. Gil, C. Ribeiro, **"Disruptive Future of Radar Based on All-Digital PN Signal Processing"**, *IEEE-APS Conference on Antennas and Propagation for Wireless Communications - APWC*, Granada, Spain, September, 2019;

Technical Report:

- R. F. S. Caldeirinha, A. Sardo, B. Tribovane, N. Leonor, **"Agile Radio Channel Sounder for 5G Propagation Modelling at mmWave Frequencies"**, *Inclusive Radio Communication Networks for 5G and beyond - IRACON*, Dublin, Ireland, January, 2019

6.3 FUTURE WORK

Future development and study of the implemented radar can be done by performing further measurements on mobile targets to evaluate their velocity by analysing *Doppler* shifts, as well as FMCW interference testing, where both radars are transmitting simultaneously, measuring the effects each have on the other.

Consideration should be given to a scenario with multiple STDCC radars, where every radar transmits a sequence that is orthogonal between each other and verifying that no interference should occur due to the auto-correlation properties of such sequences.

Target identification algorithms can be developed, as well as target tracking algorithms, by simultaneously storing and analysing the acquired data as it is being received.

A calibration algorithm can be implemented, which would be performed whenever a new measurement scenario is chosen, in order to mitigate static reflective targets and focus on mobile ones instead.

This page is intentionally left blank.

BIBLIOGRAPHY

[1] A. Bourdoux, K. Parashar, and M. Bauduin, "Phenomenology of mutual interference of FMCW and PMCW automotive radars," in *2017 IEEE Radar Conference (RadarConf)*. IEEE, may 2017.

[2] M. Gardill, "Automotive radar - a signal processing perspective on current technology and future systems," Middle East Technical University, Ankara, Turkey, 2019.

[3] D. Ferreira and R. F. S. Caldeirinha, "STDCC sounder - IF, estágio IF de uma sonda de canal rádio escalável usando o método da correlação deslizante em tempo-real," Master's thesis, Escola Superior de Tecnologia e Gestão - Instituto Politécnico de Leiria, 2010.

[4] ——, "Development and performance assessment of a real time high-resolution rf channel sounder," in *2011 IEEE International Geoscience and Remote Sensing Symposium*. IEEE, jul 2011.

[5] ——, "Development and performance analysis of a real time high-resolution channel sounder - if stage," in *2011 IEEE EUROCON - International Conference on Computer as a Tool*. IEEE, apr 2011.

[6] ——, "Development and implementation of a real time high-resolution channel sounder - if stage," in *2011 IEEE 73rd Vehicular Technology Conference (VTC Spring)*. IEEE, may 2011.

[7] D. Ferreira, R. F. Caldeirinha, and N. Leonor, "Real-time high-resolution radio frequency channel sounder based on the sliding correlation principle," *IET Microwaves, Antennas & Propagation*, jan 2015.

[8] M. I. Skolnik, *Radar Handbook*, 3rd ed., ser. Electronics electrical engineering, M. I. Skolnik, Ed. McGraw-Hill Education, 2008.

[9] P. Bello, "Characterization of randomly time-variant linear channels," *IEEE Transactions on Communications*, vol. 11, no. 4, pp. 360–393, dec 1963.

[10] J. Parsons and A. Bajwa, "Wideband characterisation of fading mobile radio channels," *IEE Proceedings F Communications, Radar and Signal Processing*, vol. 129, no. 2, p. 95, 1982.

[11] "Federal Standard 1037C: Telecommunications: Glossary of Telecommunication Terms," General Services Administration, 1996.

[12] C. R. Anderson, "Design and implementation of an ultrabroadband millimeter-wavelength vector sliding correlator channel sounder and in-building multipath measurements at 2.5 & 60 ghz," Master's thesis, Virginia Polytechnic Institute and State University, 2002.

[13] T. Rappaport, *Wireless communications: Principles and practice*, 2nd ed., ser. Prentice Hall communications engineering and emerging technologies series. Prentice Hall, 2002, includes bibliographical references and index.

[14] M. C. Jeruchim, P. Balaban, and K. Shanmugan, *Simulation of Communication Systems*. Kluwer Academic Publishers, 2002.

[15] T. Rappaport, S. Seidel, and R. Singh, "900-MHz multipath propagation measurements for US digital cellular radiotelephone," *IEEE Transactions on Vehicular Technology*, vol. 39, no. 2, pp. 132–139, may 1990.

[16] G. R. MacCartney and T. S. Rappaport, "A flexible millimeter-wave channel sounder with absolute timing," *IEEE Journal on Selected Areas in Communications*, vol. 35, no. 6, pp. 1402–1418, jun 2017.

[17] M. Lei, J. Zhang, T. Lei, and D. Du, "28-GHz indoor channel measurements and analysis of propagation characteristics," in *2014 IEEE 25th Annual International Symposium on Personal, Indoor, and Mobile Radio Communication (PIMRC)*. IEEE, sep 2014.

[18] J. Lee, J. Liang, M.-D. Kim, J.-J. Park, B. Park, and H. K. Chung, "Measurement-based propagation channel characteristics for millimeter-wave 5g giga communication systems," *ETRI Journal*, vol. 38, no. 6, pp. 1031–1041, dec 2016.

[19] E. L. Cid, M. G. Sanchez, and A. V. Alejos, "High speed transmission at 60 GHz for 5g communications," in *2015 IEEE International Symposium on Antennas and Propagation & USNC/URSI National Radio Science Meeting*. IEEE, jul 2015.

[20] E. L. Cid, M. P. Taboas, M. G. Sanchez, and A. V. Alejos, "Microcellular radio channel characterization at 60 GHz for 5g communications," *IEEE Antennas and Wireless Propagation Letters*, vol. 16, pp. 1476–1479, 2017.

[21] R. Zhang, S. Wang, X. Lu, W. Duan, and L. Cai, "Two-dimensional DoA estimation for multipath propagation characterization using the array response of PN-sequences," *IEEE Transactions on Wireless Communications*, vol. 15, no. 1, pp. 341–356, jan 2016.

[22] R. Zhang, L. Cai, Z. Zhong, J. Zhao, and J. Zhou, "Cross-polarized three-dimensional channel measurement and modeling for small-cell street canyon scenario," *IEEE Transactions on Vehicular Technology*, vol. 67, no. 9, pp.

7969–7983, sep 2018.

[23] W. G. Newhall, "Wideband propagation measurement results, simulation models, and processing techniques for a sliding correlator measurement system," Master's thesis, Virginia Polytechnic Institute and State University, 1997.

[24] D. Cox, "Delay doppler characteristics of multipath propagation at 910 MHz in a suburban mobile radio environment," *IEEE Transactions on Antennas and Propagation*, vol. 20, no. 5, pp. 625–635, sep 1972.

[25] W. Newhall, T. Rappaport, and D. Sweeney, "A spread spectrum sliding correlator system for propagation measurements," pp. 40–54, 4 1996.

[26] J. Parsons, *The mobile radio propagation channel*. Halsted Press, 1992.

[27] R. J. Pirkl and G. D. Durgin, "Optimal Sliding Correlator Channel Sounder Design," *IEEE Transactions on Wireless Communications*, vol. 7, no. 9, pp. 3488–3497, Sep. 2008.

[28] Qorvo, "RF2052 Datasheet." [Online]. Available: https://www.qorvo.com/products/d/da000363

[29] S. R. Systems, "PRS10 Datasheet." [Online]. Available: https://www.thinksrs.com/downloads/pdfs/catalog/PRS10c.pdf

[30] A. Devices, "Data Pattern Generator 2 Wiki." [Online]. Available: https://wiki.analog.com/resources/eval/dpg/dpg2

[31] ——, "AD9739 Datasheet." [Online]. Available: https://www.analog.com/media/en/technical-documentation/data-sheets/AD9739.pdf

[32] Miteq, "AM-1607 Series Datasheet." [Online]. Available: https://nardamiteq.com/docs/MITEQ-AM-1607.PDF

[33] Mini-Circuits, "SLP-1200+ Datasheet." [Online]. Available: https://ww2.minicircuits.com/pdfs/SLP-1200+.pdf

[34] Miteq, "DM0408LW2 Datasheet." [Online]. Available: https://nardamiteq.com/docs/MITEQ-DM0408.PDF

[35] Mini-Circuits, "VHF-4600+ Datasheet." [Online]. Available: https://ww2.minicircuits.com/pdfs/VHF-4600+.pdf

[36] A. Devices, "HMC-C009 Datasheet." [Online]. Available: https://www.analog.com/media/en/technical-documentation/data-sheets/hmc-c009.pdf

[37] Miteq, "AM-1469 Series Datasheet." [Online]. Available: https://nardamiteq.com/docs/MITEQ-AM-1469%20SERIES.PDF

[38] Mini-Circuits, "ZFM-2+ Datasheet." [Online]. Available: https://ww2.minicircuits.com/pdfs/ZFM-2.pdf

[39] ——, "ZFSC-2-2500 Datasheet." [Online]. Available: https://ww2.minicircuits.com/pdfs/ZFSC-2-2500+.pdf

[40] X-Microwave, "X-MWblocks." [Online]. Available: https://www.xmicrowave.com/product-category/x-mwblocks/

[41] R. Feger, H. Haderer, H. Jalli Ng, and A. Stelzer, "Realization of a Sliding-Correlator-Based Continuous-Wave Pseudorandom Binary Phase-Coded Radar Operating in W-Band," *IEEE Transactions on Microwave Theory and Techniques*, vol. 64, no. 10, pp. 3302–3318, Oct 2016.

[42] X. Corporation, "Xilinx Kintex-7 FPGA KC705 Evaluation Kit." [Online]. Available: https://www.xilinx.com/products/boards-and-kits/ek-k7-kc705-g.html

[43] ——, "7 Series FPGAs Clocking Resources – User Guide." [Online]. Available: https://www.xilinx.com/support/documentation/user_guides/ug472_7Series_Clocking.pdf

DECLARATION

I declare, on my honor, that the work presented in this dissertation, entitled *"Swept-time Delay Cross-Correlation Radar at 24/28 GHz"*, is original and was realised by André Ferreira Sardo (2172250) under the supervision of Professor Rafael F. S. Caldeirinha (rafael.caldeirinha@ipleiria.pt).

Leiria, April of 2020

André Ferreira Sardo